CHAPTER 4

TENSILE BEHAVIOUR

In this chapter, we present the influence of austempering time on the hardness and tensile behaviour of high carbon high silicon carbide-free nanostructured bainitic steel at room temperature. Additionally, we compare the results with a patented steel of the same compositions. This study provides crucial insights into the mechanical behaviour of carbide-free nanostructured bainitic steel samples, specifically highlighting the impact of a higher volume fraction of retained austenite combined with bainite. The findings presented herein are highly valuable and hold the potential to significantly contribute to the design and optimization of manufacturing processes for high-performance applications that experience monotonic loading conditions.

4.1 HARDNESS

The average Vickers hardnesses of austempered samples B12VA-1 and B12VA-2 are 524±6 HV and 590±8, respectively. The material B14VA-1 and B14VA-2 depict the average Vickers hardness of 509±7 HV and 560±9 HV, respectively. Average Vickers hardnesses of B15VA-1and B15VA-2 are 602±3 HV and 619±7 HV, respectively (Figure 4.1 & Table 4.1). It was found that the bulk hardness of the samples increased with transformation time. The average hardnesses of patented samples P12VA, P14VA and P15VA are 441±7 HV, 435±8 HV and 450±6 HV, respectively as depicted in Figure 4.1 and Table 4.1.

The average hardnesses of tensile fractured samples B12VA-1′, B12VA-2′, B14VA-1′, B14VA-2′, B15VA-1′ and B15VA-2′ are 550±7 HV, 635±4 HV, 530±5 HV, 585±6 HV, 701±6 HV and 710±9 HV, respectively.

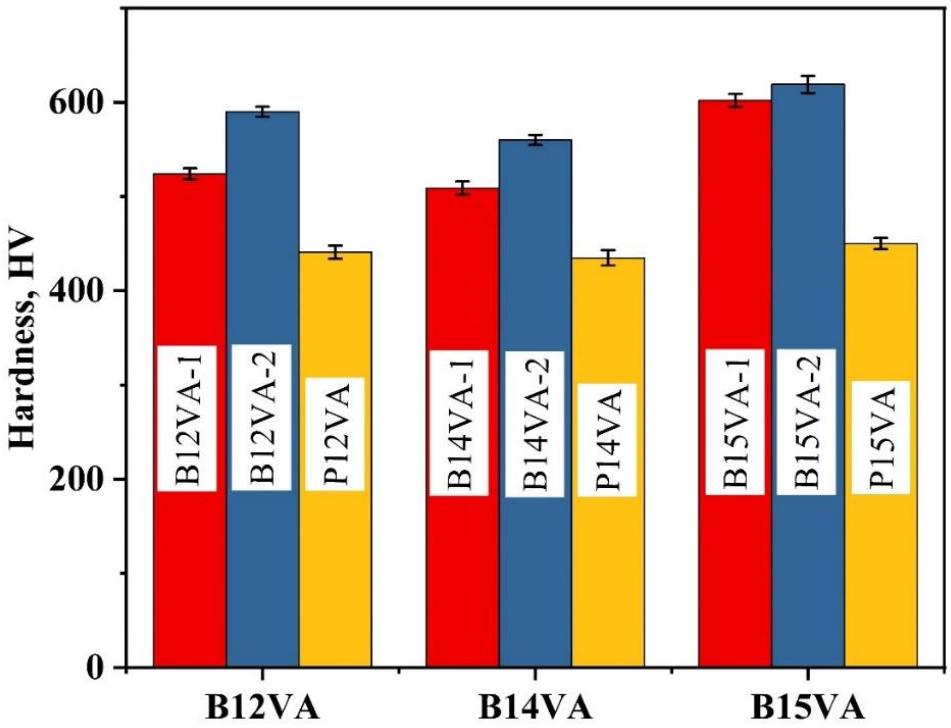

Figure 4.1 Variation of Vickers hardness measured at 10 kgf of austempered and patented steels.

4.2 TENSILE BEHAVIOUR

Figure 4.2 illustrates the engineering stress versus engineering strain diagrams of various steel samples, including austempered steels (B12VA-1, B12VA-2, B14VA-1, B14VA-2, B15VA-1, and B15VA-2) and patented steels (P12VA, P14VA, and P15VA). The data indicate the 0.2% offset proof stress or yield strength (YS) and ultimate tensile strength (UTS) of each sample. Specifically, sample B12VA-1 exhibits a YS of 878±15 MPa and a UTS of 1492±28 MPa, while sample B12VA-2 shows a YS of 1351±25 MPa and a UTS of 1727±35 MPa (Table 4.1). Sample B14VA-1 has a YS of 996±19 MPa and a UTS of 1554±31 MPa, whereas sample B14VA-2 displays a YS of 1200±22 MPa and a UTS of 1582±29 MPa. Additionally, sample B15VA-1 demonstrates a YS of 1281±40 MPa and a remarkable UTS of 1889±45 MPa, while sample B15VA-2 possesses a YS of 1428±35 MPa and a UTS of 1742±30 MPa (Table 4.1). The YS and UTS of alloys B12VA

and B14VA increase with increasing austempering time. The comparison between B15VA-1 and B15VA-2 reveals that B15VA-1 has a higher UTS, but B15VA-2 exhibits a higher YS. The YS and UTS of patented steel sample P12VA are 1062±15MPa and 1348±17 MPa, respectively. Sample P14VA has a YS of 913±13 MPa and a UTS of 1264±14 MPa whereas the sampe P15VA has a YS of 1064±12 MPa and a UTS of 1442±19 MPa. It is noteworthy that all samples share a similar Young's modulus (E) value of 190 GPa (Table 4.1).

The sample B12VA-1 shows total elongation (TE) of 14.3±0.6%, uniform elongation (UE) of 14.2±0.7% (Table 4.1) and negligible elongation after necking to fracture whereas sample B12VA-2 displays TE of 25.4±0.5% and UE of 25.0±0.6% and very small amount of elongation after necking to fracture. The sample B14VA-1 shows total elongation (TE) of 13.3±0.3%, uniform elongation (UE) of 13.3±0.3% and negligible elongation after necking to fracture whereas sample B14VA-2 displays TE of 28.3±0.7% and UE of 28.2±0.5% and very little elongation after necking to fracture. The sample B15VA-1 shows TE of 29.2±0.5%, UE of 25.0±0.6% and elongation after necking to fracture of 4.2±0.5%. The sample B15VA-2 displays TE of 18.7±0.6%, UE of 14.8±0.5%, and elongation after necking to fracture of 4.0±0.4%. The TE and UE of patented steel sample P12VA are 5.7±0.6% and 5.7±0.6%, respectively whereas the P14VA has TE and UE of 10.5±0.5% and 10.5±0.5%. The material P15VA shows TE and UE of 8.7±0.6% and 8.7±0.6% (Table 4.1). The patented steel delivers nrgligible elongation after necking.

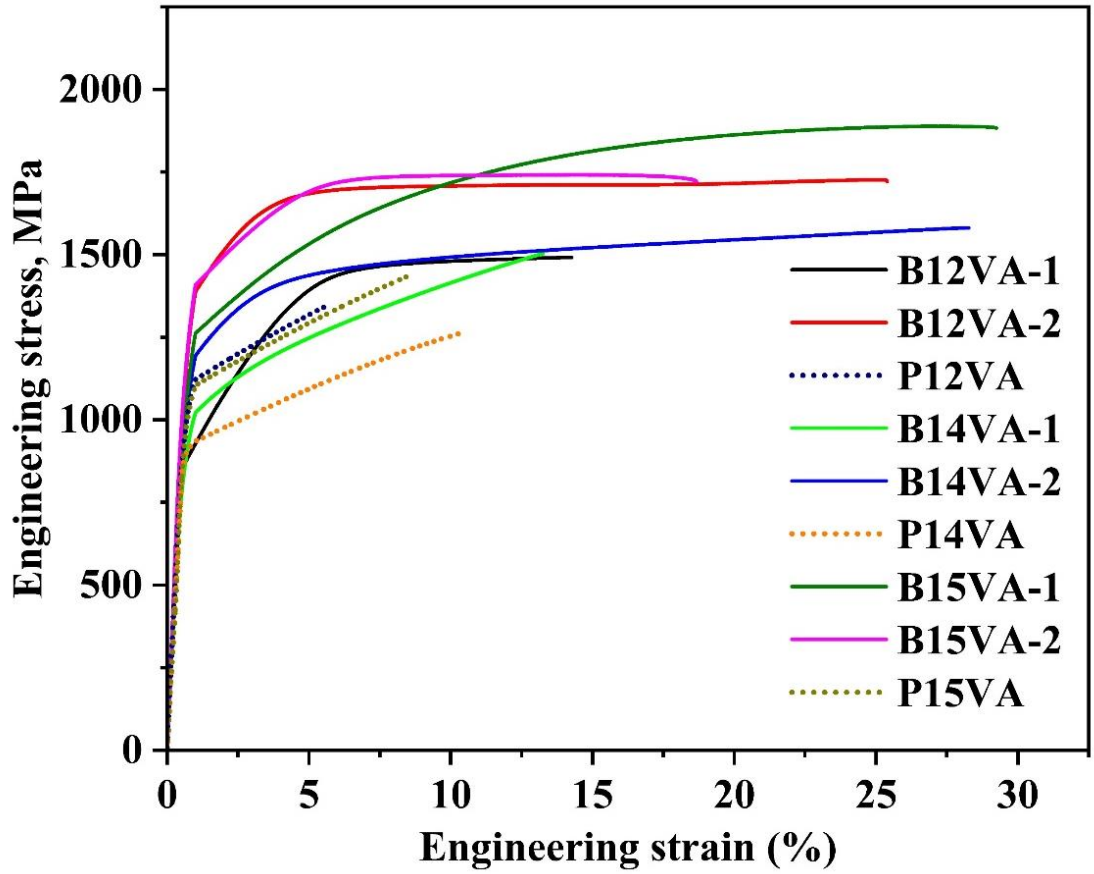

Figure 4.2 Engineering stress-strain curves of austempered steels: B12VA-1, B12VA-2, B14VA-1, B14VA-2, B15VA-1 and B15VA-2 and patented steels: P12VA, P14VA and P15VA.

The tensile toughness (U_T) of austempered samples B12VA-1, B12VA-2, B14VA-1, B14VA-2, B15VA-1 and B15VA-2 are 188±10 MJ/m^3, 414±15 MJ/m^3, 162±8 MJ/m^3, 410±11 MJ/m^3, 492±14 MJ/m^3 and 299±12 MJ/m^3, respectively (Table 4.1). The patented steels P12VA, P14VA and P15VA samples depict the tensile toughness of 61±4 MJ/m^3, 108±5 MJ/m^3 and 101±5 MJ/m^3 (Table 4.1). The material B15VA-1 shows highest tensile toughness among the steels. The sample B12VA-1 shows product of strength and elongation (PSE) value of 21.34 GPa% where as B12VA-2 shows a PSE value of 43.87 GPa%. The sample B14VA-1 displays a PSE value of 20.67 GPa% where as B14VA-2 sample shows a PSE value of 44.77 GPa%. The sample B15VA-1 displays

a highest PSE value of 55.16 GPa% where as B15VA-2 shows a PSE value of 32.57 GPa% (Table 4.1).

Table 4.1 Mechanical properties of austempered and patented steels.

Alloys	Y.S. (MPa)	U.T.S. (MPa)	TE (%)	UE (%)	U_T (MJ/m3)	PSE (GPa%)	Hardness (HV)
B12VA-1	878±15	1492±28	14.3±0.6	14.2±0.7	188±10	21.34	524±6
B12VA-2	1351±25	1727±35	25.4±0.5	25.0±0.6	414±15	43.87	590±8
B14VA-1	996±19	1554±31	13.3±0.3	13.3±0.3	162±8	20.67	509±7
B14VA-2	1200±22	1582±29	28.3±0.7	28.2±0.5	410±11	44.77	560±5
B15VA-1	1281±27	1889±40	29.2±0.5	25.0±0.6	492±14	55.16	602±7
B15VA-2	1428±23	1742±35	18.7±0.7	14.8±0.5	299±12	32.58	619±9
P12VA	1062±15	1348±17	5.7±0.6	5.7±0.6	61±4	7.68	441±7
P14VA	913±13	1264±14	10.5±0.5	10.5±0.5	108±5	13.27	435±8
P15VA	1064±12	1442±19	8.7±0.6	8.7±0.6	101±5	12.55	450±6

The true stress-true strain behaviour of the austempered steel samples are shown in Figure 4.3. The flow stress corresponding to UTS in sample B12VA-1 is 1704 MPa and the total true strain is 13.3% whereas the sample B12VA-2 has flow stress corresponding to UTS of 2158 MPa and total true strain of 22.6%. The sample B14VA-1 has a flow stress corresponding to UTS of 1701 MPa and total true strain of 12.5%, whereas the sample B14VA-2 sample has a flow stress of 2028 MPa and total true strain of 24.9%. The flow stress corresponding to UTS in sample B15VA-1 is 2396 MPa and the total true strain(ε) is 23.8% whereas the B15VA-2 data reveal flow stress of 1999 MPa at UTS and a total true strain of 13.8%. Flow stress increases with the true strain and shows better strain hardening in sample B15VA-1 as compared to sample B15VA-2. The samples B12VA-1, B12VA-2, B14VA-1, B14VA-2 and B15VA-1 displays three slopes in the plastic strain indicating three stages of work hardening behaviour.

The strain at which slopes are changed are indicated by numbers 1-3 on σ-ε curve. The sample B15VA-2 also displays three slopes of three stages but there are transition zones where slopes are variable and strain positions are marked by 1-1' and 2-2' (Figure 4.3).

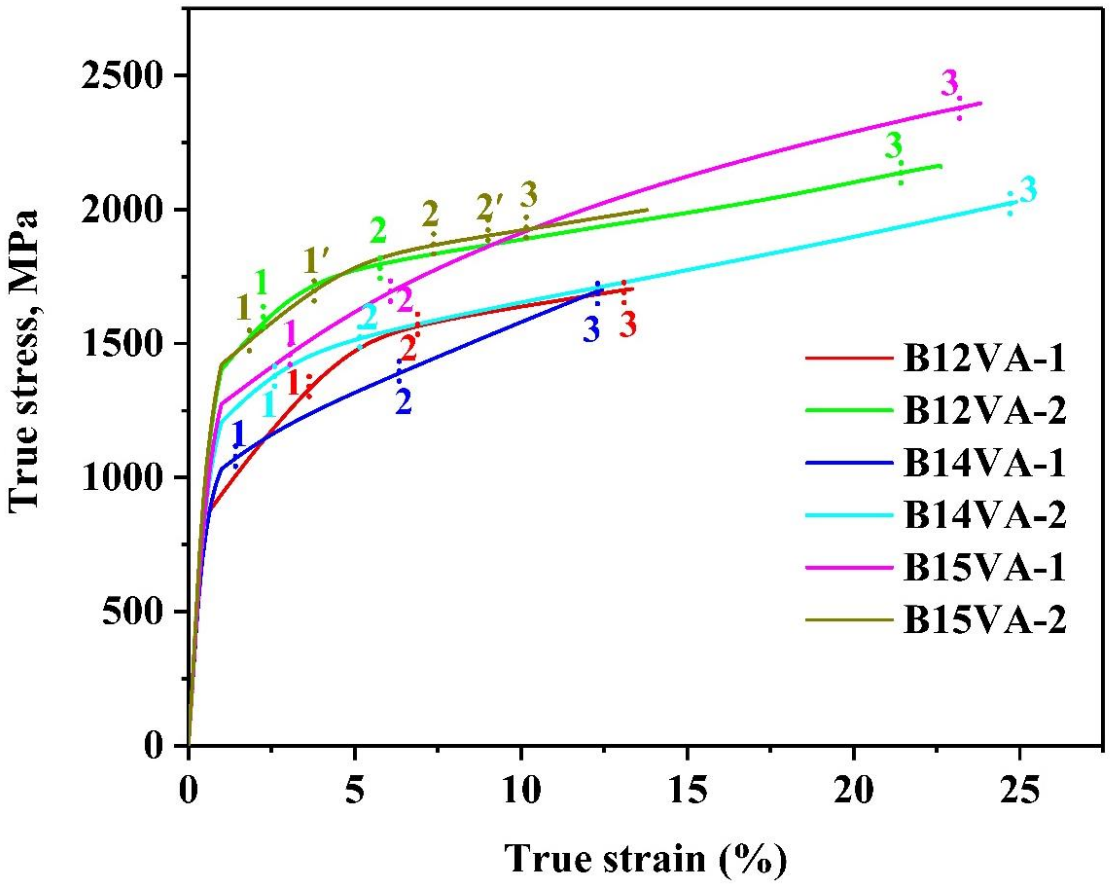

Figure 4.3 True stress-true strain curves of austempered samples. Number 1-3 on the graph indicates the change in slope of the work hardening rate.

4.3 TENSILE FRACTURE BEHAVIOUR

Figure 4.4a displays SEM secondary electron images of fracture surface (fractography) of B12VA-1′. It shows a high amount of cleavage facets surrounded by tearing ridges and negligible dimples whereas sample B12VA-2′ depicts the presence of large amount of cleavage facets surrounded by tearing ridges and small amount of micro dimples of sizes 0.6±0.13 μm (Figure 4.4b). The material B12VA-1' shows brittle

fracture. Figure 4.4c shows the SEM fractographs of B14VA-1′ and it reveals very large amount of cleavage facets surrounded with tearing ridges and negligible dimples whereas the fractographs of sample B14VA-2′ shows presence of small amount of micro-sized dimples of size 0.5±0.15 μm and heavy amount of tearing ridges also, large amount of cleavage facets surrounded with tearing ridges were seen.

In Figure 4.4e, the SEM image of the fracture surface of B15VA-1' reveals a significant number of dimples, with an average size of 4.45±1.7 μm. These dimples indicate that the material underwent ductile fracture, characterized by plastic deformation. Additionally, there are a few smaller micro dimples, averaging 0.9±0.24 μm in size. Tearing ridges are also observed, suggesting the occurrence of tearing during the fracture process. Cleavage facets are present, albeit in a very small number. Figure 4.4b depicts the SEM fractographs of B15VA-2' exhibit some differences compared to B15VA-1'. The dimples are smaller, with an average size of 2.3±0.57 μm, indicating a more localized plastic deformation during fracture. There is an increased occurrence of micro dimples, averaging 0.5±0.18 μm in size. Tearing ridges are also present. Furthermore, approximately 4% of the area shows cleavage facets, suggesting a slight shift towards a more brittle fracture behaviour compared to B15VA-1'.

Tensile fractographs of the patented steel samples are depicted in Figure 4.5a-c for P12VA′, P14VA′ and P15VA′, respectively. Fractography reveals the presence of cleavage facets surrounded by tearing ridges. Brittle fracture behaviour is observed in patented steel samples.

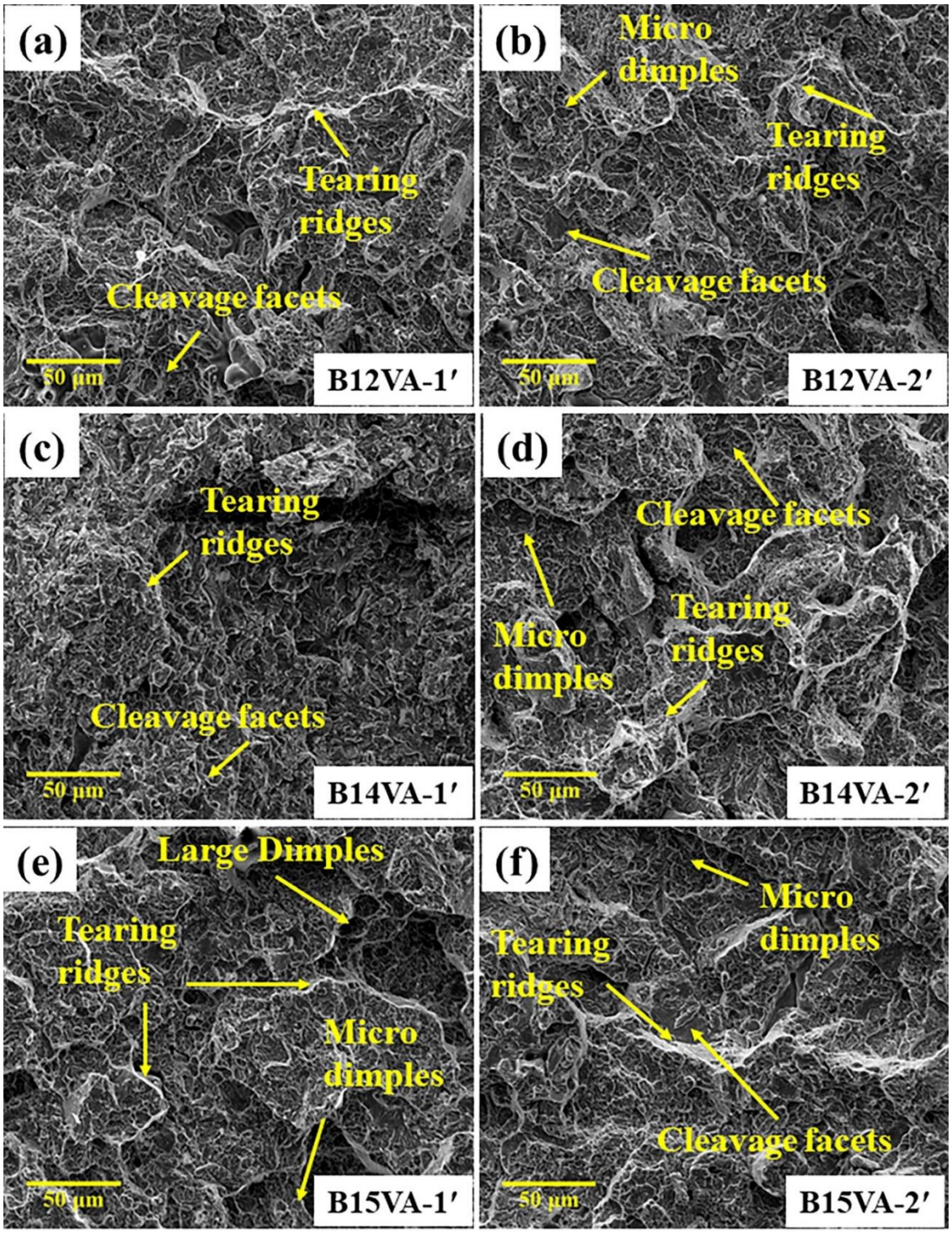

Figure 4.4 SEM fractographs of samples austempered at 250°C (a) B12VA-1′, (b) B12VA-2′, (c) B14VA-1′, (d) B14VA-2′, (e) B15VA-1′ and (f) B15VA-2', respectively.

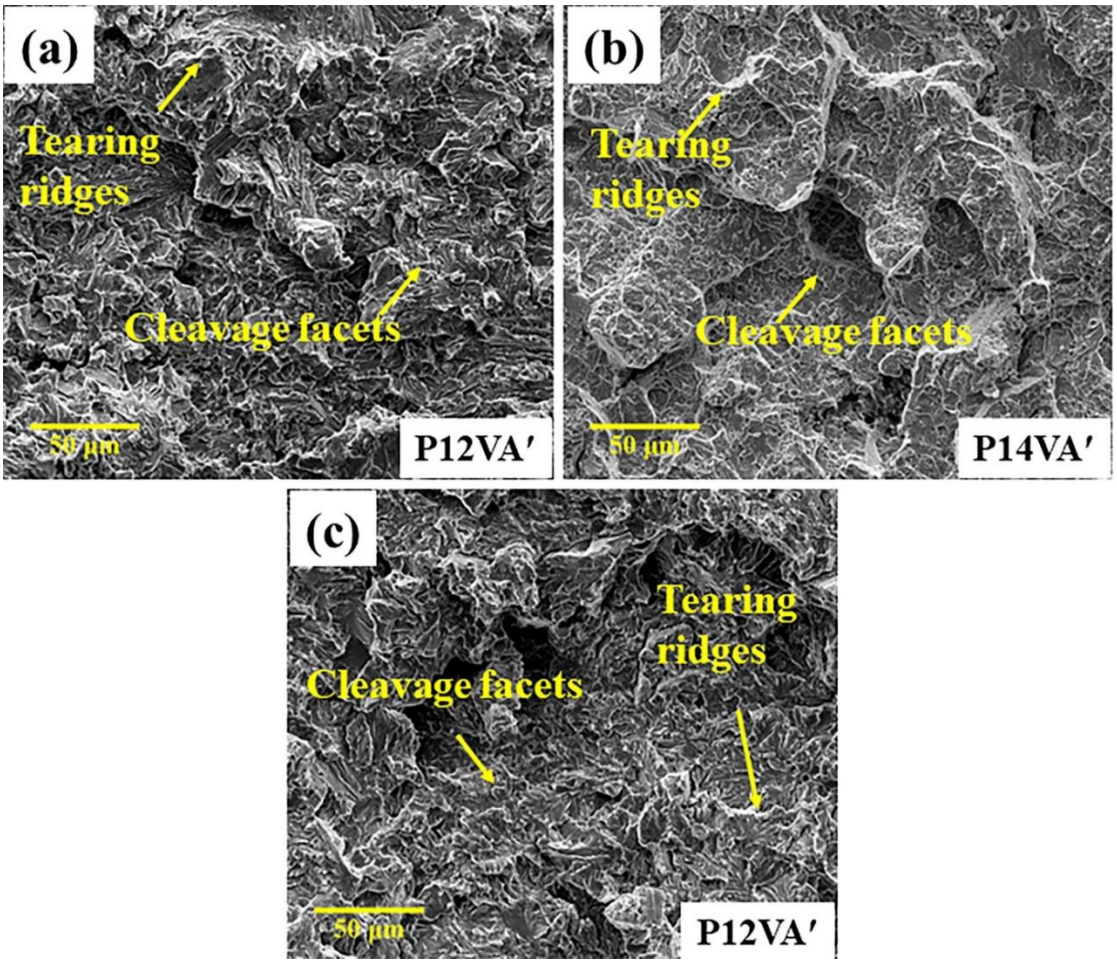

Figure 4.5 SEM fractographs of samples patented at 550°C (a) P12VA′, (b) P14VA′ and (c) P15VA', respectively.

4.4 STRAIN-INDUCED MARTENSITIC TRANSFORMATION

4.4.1 X-Ray Diffraction Study of Tensile Tested Samples

Figure 4.6a shows the XRD pattern of tensile tested sample B12VA-1 (B12VA-1′). The XRD pattern displays the peak intensity of retained austenite, bainite and new phase of BCT martensite without any carbide. The calculated crystallite size of retained austenite and bainite decreases from 46.2 nm to 20.7 nm and 42.1 nm to 25.3 nm, respectively (Table 4.2). The lattice strain of retained austenite and bainite increases from 0.28% to 0.52% and 0.30% to 0.43%, respectively (Table 4.2). The dislocation density of retained austenite and bainite increases from 8.28 x10^{16}/m^2 to 33.86 x10^{16}/m^2 and 9.78

x10^{16}/m^2 to 23.74 x10^{16}/m^2 (Table 4.2). The volume fraction of retained austenite of the fractured tensile sample B12VA-1′ decreases from 48% to 41% and the XRD pattern reveals about 7% α′-martensite (V_M) and the evaluated volume fraction of filmy austenite and blocky austenite are 7.8% and 33.2%, respectively.

Figure 4.6b illustrates the XRD pattern obtained from the tensile tested sample B12VA-2 (referred to as B12VA-2′). The XRD pattern reveals the intensity of peaks corresponding to retained austenite, bainite, and a new phase known as BCT martensite, with no indication of carbide presence. Upon analysis, it was found that the crystallite size of retained austenite and bainite decreased from 35.7 nm to 16.8 nm and 36.4 nm to 24.2 nm, respectively (Table 4.2). The lattice strain of retained austenite and bainite exhibited an increase from 0.35% to 0.63% and 0.33% to 0.44%, respectively (Table 4.2). Furthermore, the dislocation density of retained austenite and bainite experienced an increase from 13.10 x 10^{16}/m^2 to 50.54 x 10^{16}/m^2 and 12.66 x 10^{16}/m^2 to 25.39 x 10^{16}/m^2, respectively (Table 4.2). As for the fractured tensile sample B12VA-2′, the volume fraction of retained austenite decreased from 35% to 26%. Analysis of the XRD pattern revealed the presence of approximately 9% α′-martensite, and the evaluated volume fractions indicated 9.8% for filmy austenite and 16.2% for blocky austenite.

In Figure 4.6c, the XRD pattern of tensile tested sample B14VA-1 (referred to as B14VA-1′) is presented, showcasing the peak intensity of retained austenite, bainite, and a new BCT martensite phase, with no evidence of carbides. Notably, the crystallite size of retained austenite and bainite has undergone a reduction, decreasing from 85.8 nm to 22.0 nm and 40.7 nm to 22.8 nm, respectively (Table 4.2). Simultaneously, the lattice strain of retained austenite and bainite has increased, rising from 0.17% to 0.49% and 0.30% to 0.47%, respectively (Table 4.2). Additionally, the dislocation density in retained

austenite and bainite has experienced an increment, ascending from 2.64 x $10^{16}/m^2$ to 30.08 x $10^{16}/m^2$ and 10.39 x $10^{16}/m^2$ to 28.79 x $10^{16}/m^2$ (Table 4.2). Furthermore, the volume fraction of retained austenite in the fractured tensile sample B14VA-1′ has decreased from 67% to 58%. The XRD pattern analysis indicates the presence of approximately 9% α′-martensite, while the evaluated volume fractions of filmy austenite and blocky austenite are 6.8% and 51.2%, respectively.

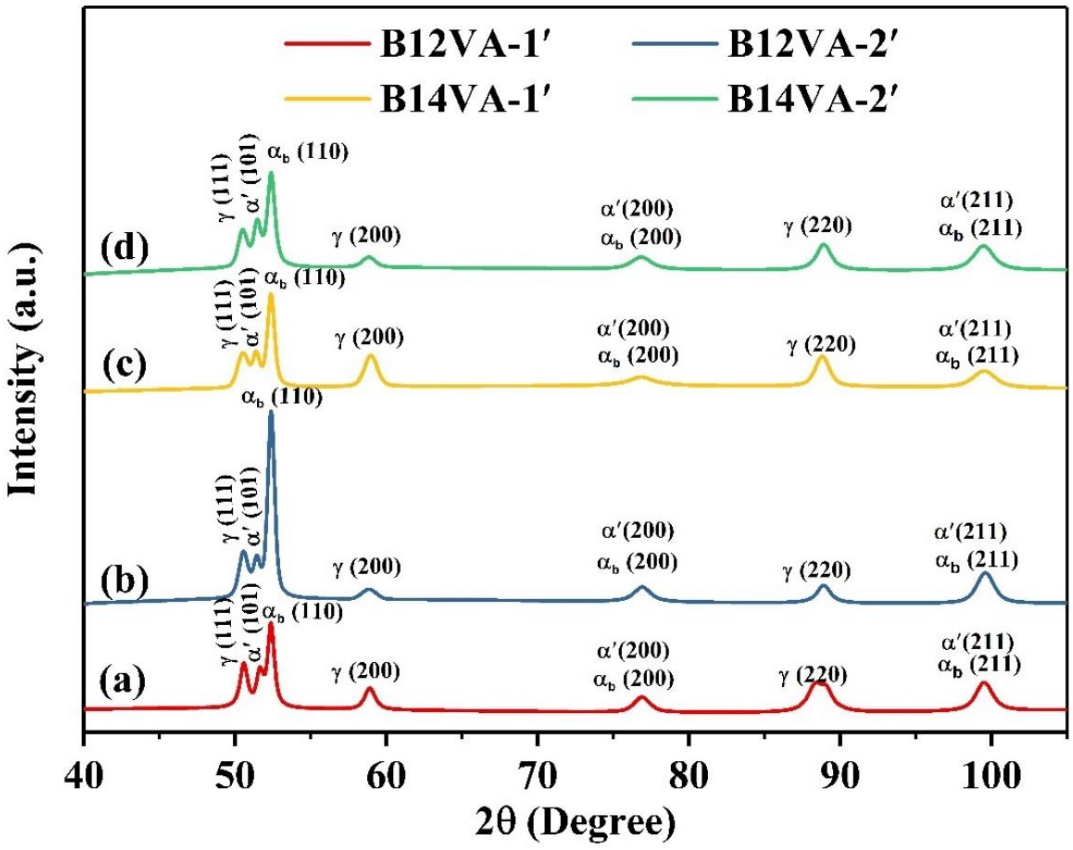

Figure 4.6 X-ray diffraction patterns of tensile fractured samples: (a) B12VA-1′, (b) B12VA-2′, (c) B14VA-1′ and (d) B14VA-2′.

The XRD pattern displayed in Figure 4.6d depicts the results of the tensile test conducted on sample B14VA-2 (also known as B14VA-2′). The pattern reveals the peak intensities corresponding to retained austenite, bainite, and a newly formed BCT martensite phase, with no detectable presence of carbides. The analysis of the XRD data

demonstrates a decrease in the crystallite size of retained austenite from 30.0 nm to 17.2 nm, while for bainite, the decrease is from 37.8 nm to 21.5 nm (Table 4.2). Concurrently, the lattice strain of retained austenite increases from 0.40% to 0.62%, and for bainite, it increases from 0.32% to 0.49%. Moreover, the dislocation density of retained austenite shows an increase from 17.92 x $10^{16}/m^2$ to 48.58 x $10^{16}/m^2$, while for bainite, it increases from 11.82 x $10^{16}/m^2$ to 31.83 x $10^{16}/m^2$. In the fractured tensile sample B14VA-2′, there is a decrease in the volume fraction of retained austenite from 35% to 23%. The XRD pattern reveals the presence of approximately 12% α′-martensite, and the evaluated volume fractions of filmy austenite and blocky austenite are 9.75% and 13.33%, respectively.

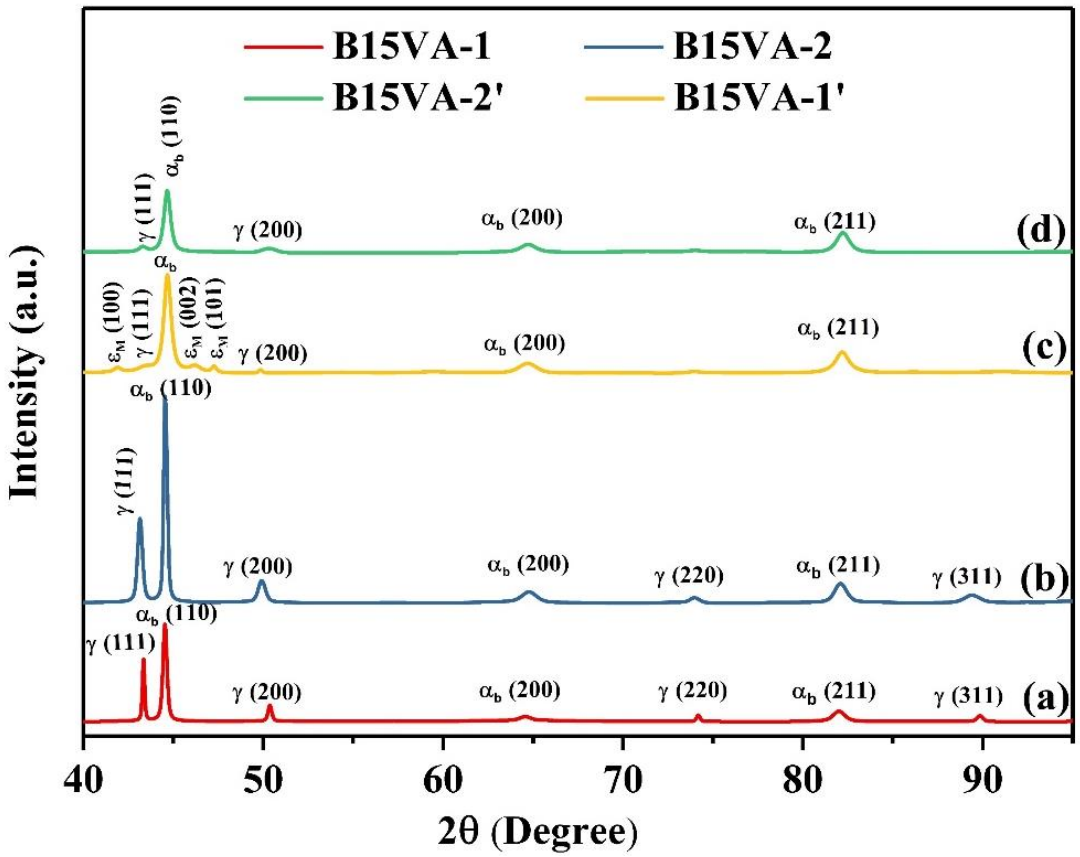

Figure 4.7 X-ray diffraction patterns of the austempered and the tensile fractured samples: (a) B15VA-1, (b) B15VA-2, (c) B15VA-1′ and (d) B15VA-2′.

Figure 4.7a and Figure 4.7b depict the XRD pattern of the austempered B15VA-1 and B15VA-2 samples. Figure 4.7c shows the XRD pattern of the tensile tested sample of B15VA-1(B15VA-1′). The pattern reveals the peak intensities of retained austenite, bainite and new phase of ε-martensite without any carbide. The calculated crystallite size of retained austenite and bainite decreases from 31.2 nm to 27.2 nm and 33.3 nm to 22.5 nm, respectively (Table 4.2). The lattice strain of retained austenite and bainite increases from 0.387% to 0.429% and 0.355% to 0.488%, respectively (Table 4.2). The dislocation density of retained austenite and bainite increases from 16.7 $x10^{16}/m^2$ to 21.3 $x10^{16}/m^2$ and 14.9 $x10^{16}/m^2$ to 30.3 $x10^{16}/m^2$ (Table 4.2). The volume fraction of retained austenite of the fractured tensile sample B15VA-1′ decreases from 45% to 9% and the XRD pattern reveals about 11% ε-martensite and the evaluated volume fraction of filmy austenite and blocky austenite are 8.25% and 0.75%, respectively (Table 4.2).

Figure 4.7d displays the XRD patterns of B15VA-2′. The pattern shows the peak intensities of retained austenite and bainite but no peaks of ε-martensite or carbides. The calculated crystallite size of retained austenite and bainite decreases from 28.2 nm to 20.6 nm and 30.1 nm to 25.0 nm, respectively (Table 4.2). The lattice strain of retained austenite and bainite increases from 0.419% to 0.554% and 0.385% to 0.456%, respectively (Table 4.2). The dislocation density of retained austenite and bainite increases from 20 $x10^{16}/m^2$ to 36.2 $x10^{16}/m^2$ and 17.9 $x10^{16}/m^2$ to 25.5 $x10^{16}/m^2$ (Table 4.2). The volume fraction of retained austenite of the B15VA-2′ sample decreases from 35% to 11% and the estimated volume fraction of filmy austenite and blocky austenite are 9.75% and 1.25%, respectively (Table 4.2). These findings indicate that the tensile testing induced changes in phase fractions, crystallite sizes, lattice strains, and dislocation densities of the austenite and bainite phases.

Table 4.2 Microstructural features of the tensile fractured austempered steel.

Tensile fractured Samples	V_{RA} %	V_B %	V_M %	C.S., nm		L. S., %		ρ on (111) plane ($x10^{16}/m^2$) (ϒ)	ρ on (110) plane ($x10^{16}/m^2$) (α_b)
				ϒ	α_b	ϒ	α_b		
B12VA-1′	41	52	7	20.7	25.3	0.52	0.43	33.86	23.74
B12VA-2′	26	65	9	16.8	24.2	0.63	0.44	50.54	25.39
B14VA-1′	58	33	9	22.0	22.8	0.49	0.47	30.08	28.79
B14VA-2′	23	65	12	17.2	21.5	0.62	0.49	48.58	31.83
B15VA-1′	9	55	36	14.9	23.2	0.71	0.46	64.23	27.69
B15VA-2′	11	65	24	17.0	21.4	0.63	0.49	49.95	31.98

4.4.2 EBSD analysis of Tensile Tested Samples

Electron back scattered diffraction (EBSD) analysis was utilized for the qualitative measurement of phase fraction and strain in the tensile tested samples. Figure 4.8a depicts the phase map of the sample B12VA-1′ and it reveals that there is very little change in the phase fraction of bainite, martensite and retained austenite after tensile fracture. Sample B12VA-2′ shows an increment in the phase fraction of bainite/martensite by 8% due to the strain-induced transformation of blocky retained austenite to martensite as depicted in Figure 4.8b. Figure 4.8c depicts the phase map of sample B14VA-1′ and it reveals ~9% increase in volume fraction of bainite/martensite whereas sample B14VA-2′ shows very less increase in martensite content as seen in Figure 4.8d. The phase map of sample B15VA-1′ is depicted in Figure 4.8e and it reveals an increase of phase fraction of ferrite by ~35% whereas the sample B15VA-2′ shows an increase of bainite/martensite content by 21%. The increase in martensite content confirms the strain-induced transformation from blocky austenite during tensile straining. The observed data were concurrent with the quantitative measurement by XRD.

Figure 4.9a-f depict the KAM map of the tensile fractured sample and it reveals that the strain in the austempered samples increased after tensile straining due to the formation of strain-induced martensite in the blocky austenite region.

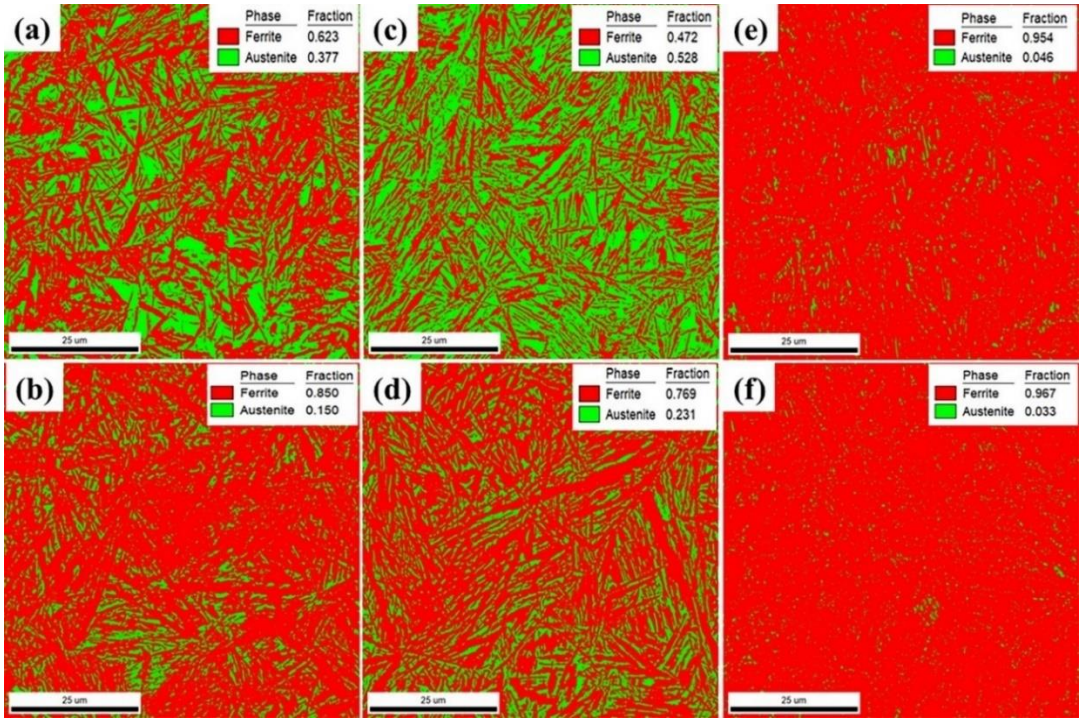

Figure 4.8 EBSD phase map of the tensile tested austempered steel: (a) B12VA-1′, (b) B12VA-2′, (c) B14VA-1′, (d) B14VA-2′, (e) B15VA-1′ and (f) B15VA-2′.

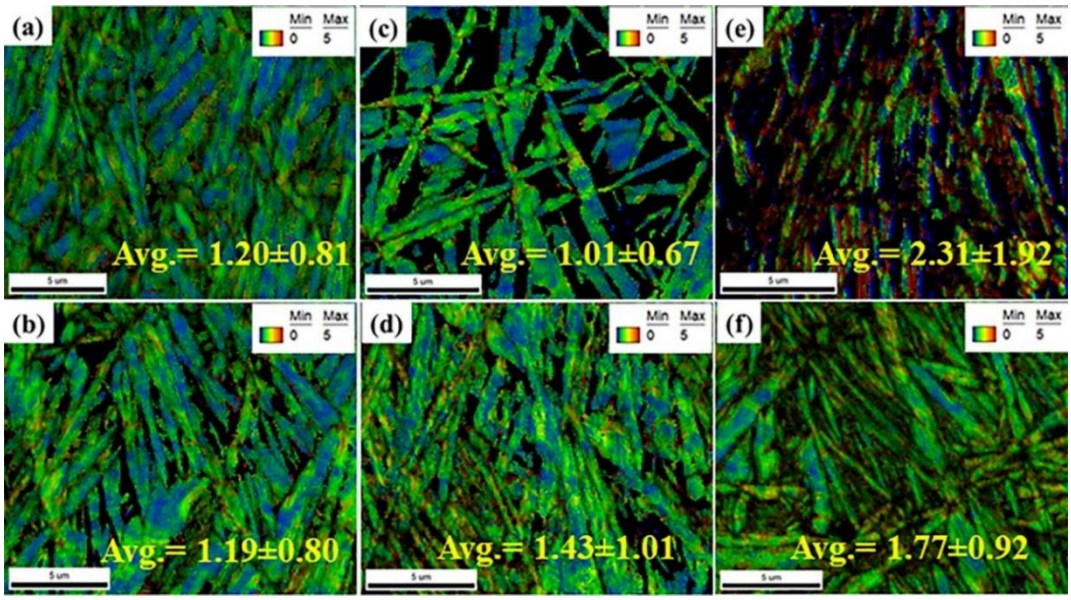

Figure 4.9 KAM maps of the tensile tested austempered steel: (a) B12VA-1′, (b) B12VA-2′, (c) B14VA-1′, (d) B14VA-2′, (e) B15VA-1′ and (f) B15VA-2′.

The image quality map of the tensile fractured sample B12VA-1′ is shown in Figure 4.10a, it reveals the presence of sheaves of bainite and blocky retained austenite along with low angle grain boundary (LAGB) and high angle grain boundary (HAGB). It is observed that percentage of LAGB increases from ~7% to ~ 13% and corresponding decrease in percentage of HAGB from ~68% to ~50% after tensile straining (IQ map of austempered samples were discussed in section 3.5 of Chapter 3). Similar type of morphology of sheaves of bainite are seen in IQ map of sample B12VA-2′ (Figure 4.10b), it also reveals increase in LAGB from ~6% to ~14% and corresponding decrease in the HAGB from ~68% to ~46%. The image quality map of sample B14VA-1', is displayed in Figure 4.10c. The map clearly reveals the presence of sheaves of bainite and blocky retained austenite, alongside LAGB and HAGB. Interestingly, the analysis demonstrates a significant increase in the percentage of LAGB from approximately 6% to about 9%, accompanied by a corresponding decrease in the percentage of HAGB from around 72% to approximately 59% after undergoing tensile straining. The IQ map of sample B14VA-2' (Figure 4.10d) exhibits a similar morphology of sheaves of bainite as observed in sample B14VA-1'. Additionally, the IQ map of B14VA-2' provides insights into the changes in grain boundaries following tensile straining. Similar to B14VA-1', an increase in the percentage of LAGB is observed, rising from approximately 6% to around 20%. In parallel, there is a corresponding decrease in the percentage of HAGB from approximately 75% to about 39%. Sample B15VA-1' undergoes tensile straining, resulting in changes to its grain boundary characteristics (Figure 4.10e). The analysis reveals an increase in LAGB from approximately 5% to about 16%, while HAGB decreases from around 69% to approximately 42.5%. The IQ map of B15VA-2' showcases (Figure 4.10f), there is a significant increase in LAGB from approximately

6% to around 24% and a corresponding decrease in HAGB from approximately 72% to about 32%. These findings highlight the impact of tensile straining on grain boundaries and the presence of consistent microstructural features in the samples.

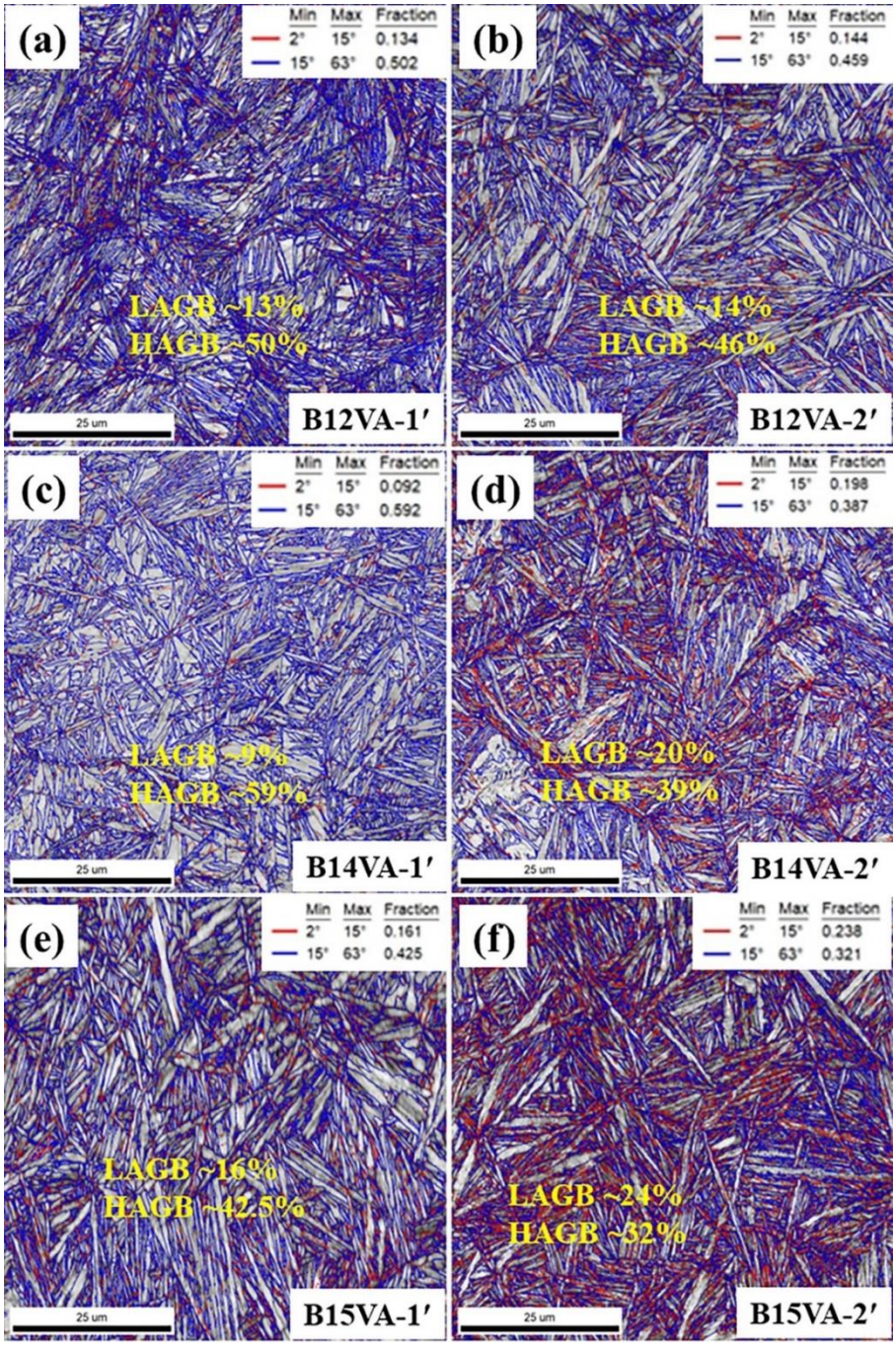

Figure 4.10 Image quality maps of the tensile fractured austempered samples along with LAGB and HAGB: (a) B12VA-1′, (b) B12VA-2′, (c) B14VA-1′, (d) B14VA-2′, (e) B15VA-1′ and (f) B15VA-2′, respectively. Fraction of the LAGB and HAGB are shown in insets.

4.4.3 TEM Study of Tensile Tested Samples

In Figure 4.11a, a TEM BFI of the fractured subsurface of B12VA-1' reveals important microstructural features. The image shows the presence of nano-scale bainite, reduced retained austenite, and newly formed strain-induced twinned martensites (α′) with a body-centered tetragonal (BCT) structure. To further investigate the α′ martensite, a selected area electron diffraction pattern (SAEDP) is taken from the α′ martensite area, which is marked by a yellow-colored square on the bright-field image. The SAED pattern confirms the presence of α′ martensite, which is formed through strain-induced martensitic (SIM) transformation when the mechanically unstable blocky retained austenite is subjected to tensile straining.Similarly, in Figure 4.11b, a TEM BFI of B12VA-2' displays fine bainite and retained austenite, along with strain-induced martensite. By examining the magnified inset of Figure 4.11b, α′ martensite is observed. The SAED pattern of the selected area in the inset further confirms the presence of α′ martensite.

Figure 4.11c presents a TEM BFI of the tensile fractured B14VA-1' sample. The BFI shows the presence of nanostructured bainite, filmy retained austenite, and newly formed strain-induced α′ martensite. The magnified inset of Figure 4.11c focuses on a selected yellow-colored rectangle, revealing the presence of α′ martensite. The SAED pattern obtained from the selected area in the inset provides additional evidence of twinned α′ martensite. Figure 4.11d presents the TEM BFI of the tensile fractured B14VA-2' sample. The image displays nanostructured bainite, filmy retained austenite, and newly formed strain-induced martensite of the body-centered tetragonal (BCT) type. The selected area within the yellow-colored rectangle highlights the α′ twinned martensite. The SAED pattern obtained from this area confirms the presence of BCT

martensite after tensile straining. In summary, the TEM BFIs provide valuable insights into the microstructures of the fractured subsurface samples. The observations indicate the presence of bainite, retained austenite, and strain-induced martensite. The formation of martensite is attributed to the strain-induced martensitic transformation occurring during the tensile straining of the samples.

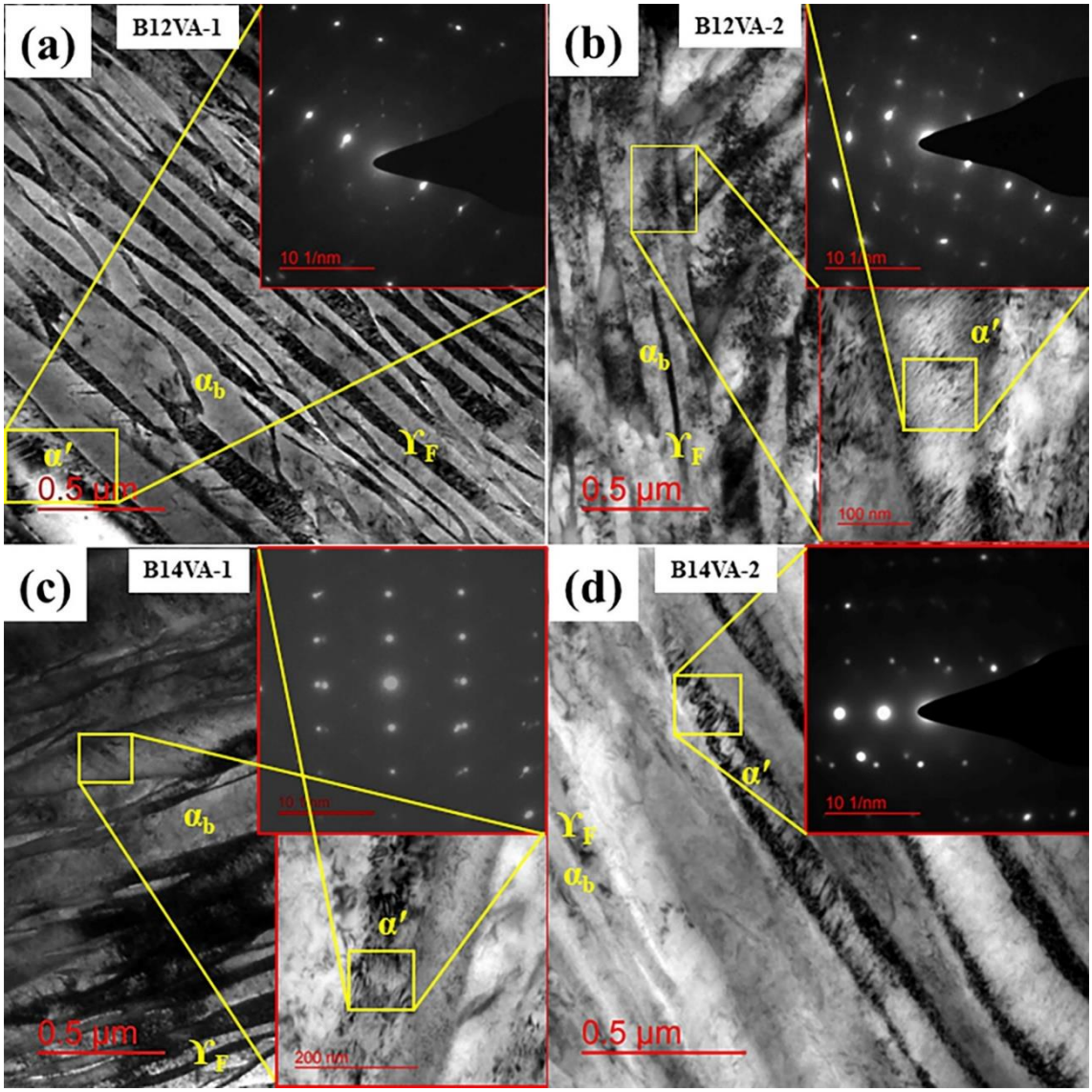

Figure 4.11 TEM bright-field images (BFI) of tensile fractured samples (a)B12VA-1', (b) B12VA-2', (c) B14VA-1' and (d) B14VA-2' sample. SAED pattern and martensites are shown as magnified insets.

Figure 4.12a provides TEM BFIs of fractured subsurface of B15VA-1′. The microstructure reveals the presence of nano-scale bainite, reduced retained austenite and newly formed strain-induced twinned martensites (ε_M, hexagonal close-packed (HCP)). Martensites are shown as magnified insets in Figure 4.12a. The TEM micrographs display intense dislocation debris (marked in red circle) along with martensite (marked in yellow circle).

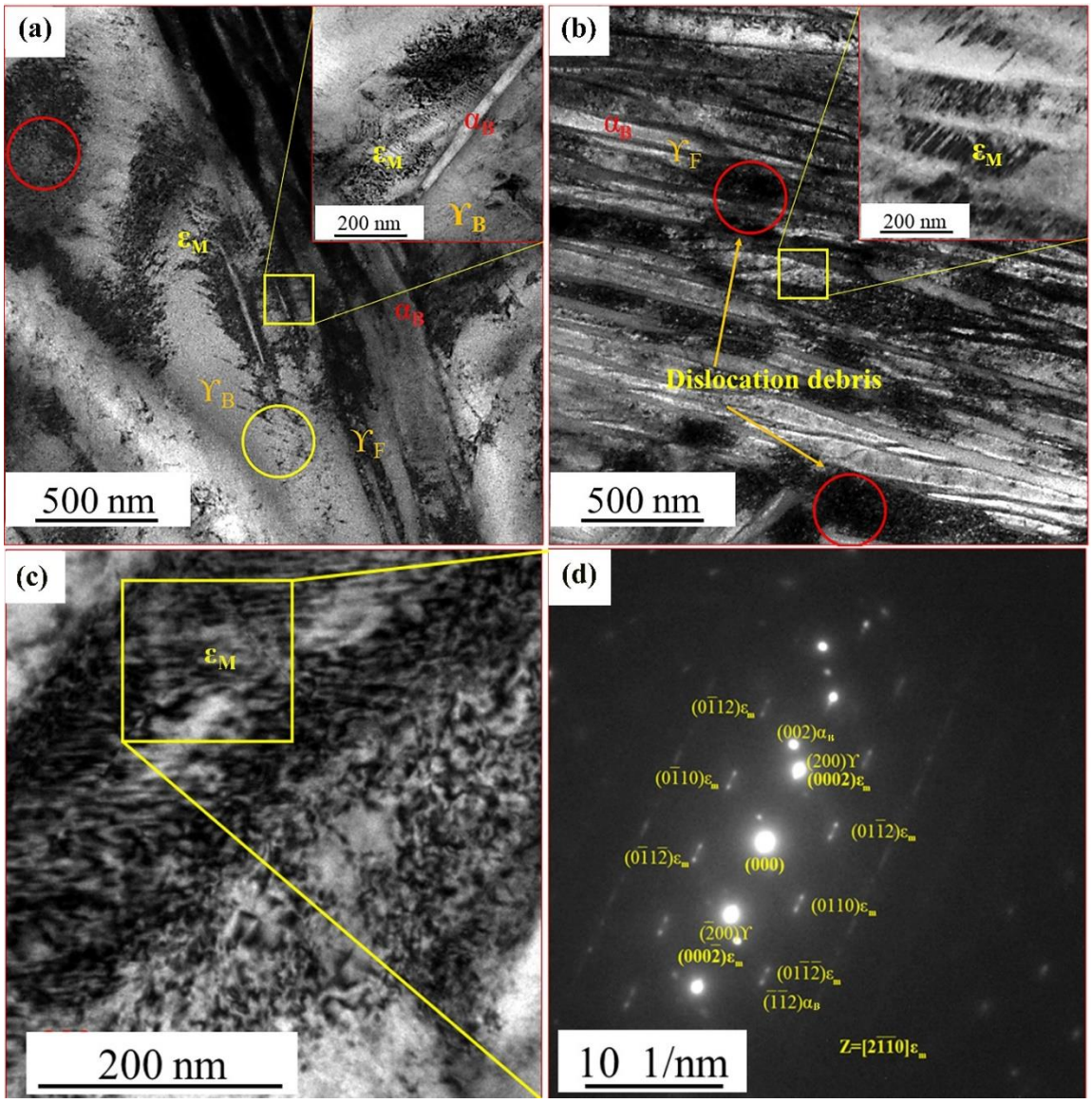

Figure 4.12 TEM bright-field images (BFI) of tensile fractured samples (a)B15VA-1', (b) B15VA-2', corresponding (c) BFI of B15VA-1' and (d) SAED pattern of B15VA-1' sample. Martensites are shown as magnified insets.

Figure 4.12b shows TEM BFI of B15VA-2′ containing fine bainite and retained austenite along with strain-induced martensite. It reveals an increase in dislocation debris after tensile straining. A selected area electron diffraction pattern (SAEDP) (Figure 4.12d) of B15VA-1′ is taken from the epsilon martensite area (marked by a square) on the new bright-field image (Figure 4.12c). The indexed SAEDP reveals the presence of epsilon martensite. These martensites are formed by strain-induced martensitic (SIM) transformation on tensile straining of mechanically unstable blocky retained austenite.

4.5 WORK HARDENING BEHAVIOUR

Various relationships for describing work hardening behaviour proposed by Hollomon, Ludwik, Swift, Ludwigson and Voce [154-158] were employed to investigate the work hardening behaviour of the austempered steel samples.

Single-sloped logarithmic work hardening behaviour in the uniform strain regime is described by Hollomon [154] and is given by Equation (4.1).

$$\sigma = K\varepsilon^n \tag{4.1}$$

Where σ is true stress, ε is true plastic strain, K is strength co-efficient and n is strain hardening exponent.

Material showing varied yield strength but similar strain hardening or similar yield strength but varied work hardening behaviour requires additional terms to describe the flow behaviour. This is achieved by introducing an additional stress term σ_o which is yielding at low strain, in the Hollomon relationship by Ludwik and the work hardening behaviour is provided by Equation (4.2) [155].

$$\sigma = \sigma_o + K\varepsilon^n \tag{4.2}$$

Where σ_o is the yield stress.

The work hardening behaviour of pre-strained material is illustrated by Swift [156] by introducing a pre-strain term (ε_o) in the Hollomon relationship and is described by Equation (4.3).

$$\sigma = K(\varepsilon_o + \varepsilon)^n \quad (4.3)$$

Ludwigson [157] analyzed that for many fcc materials having low stacking fault energy (SFE) work hardening cannot be described by Hollomon Equation but a large positive deviation in stress at low strain can be accommodated by introducing an additional term and the work hardening behaviour is given by the Equation (4.4).

$$\sigma = K\varepsilon^n + \exp(K_1 + n_1\varepsilon) \quad (4.4)$$

Where K_1 is the additional strength coefficient and n_1 is also an additional strain hardening exponent related to the additional slope region of the true stress and true strain curve.

In case of saturation in stress at higher stress/strain levels work hardening behaviour is provided by Voce [158] and is given by Equation (4.5).

$$\sigma = \sigma_s - (\sigma_s - \sigma_I)(n\varepsilon) \quad (4.5)$$

Where σ_s is the saturation stress and σ_I is true stress (yield stress).

Levenberg Marquardt iteration algorithms are used to fit equation 4.1 to 4.5 with known experimental data and plotted to find the best fit. The best fit is judged by the lowest value of chi-square (χ^2) (sum of the ratio of squares of the deviation of calculated stress values from the experimental stress values to the calculated value) and highest R-square (R^2) (coefficient of determination or goodness of fit) value. The work hardening parameters are derived by the above iteration technique from the best-fit curve/equation. Figures 4.13 to 4.15 shows the double logarithmic plots of true stress vs true plastic strain

for B12VA-1, B12VA-2, B14VA-1, B14VA-2, B15VA-1 and B15VA-2. They reveal an upward concave shape of the curve for all the samples except using Hollomon (Equation (4.1)) and Voce (Equation (4.5)). Equation (4.1) gives a linear log-log plot but Equation (4.5) provides multiple slopes which are deviated very much from experimental plots. The work hardening performance of B12VA, B14VA and B15VA alloys is analyzed by above mentioned relations to determine various work hardening parameters. The double logarithmic plot of true stress- true plastic strain curve obtained from Ludwigson relationship provides the best fit with the experimental data, with the highest R^2 values and lowest χ^2 value (Table 4.3) for B12VA-1, B12VA-2, B14VA-1 and B14VA-2 steels in comparison to respective values obtained from the Hollomon, Ludwik, Swift and Voce equations.

The strength coefficients K and K_1 derived from Ludwigson relationship for sample B12VA-1 are 7397 MPa and 6.68 MPa (Figure 4.13a), respectively whereas for the sample B12VA-2 are 2337 MPa and 0.16 MPa, respectively (Figure 4.13b and Table 4.3). The derived strain hardening exponents n and n_1 for sample B12VA-1 are 0.75 and -0.99, respectively, whereas for the sample B12VA-2 are 0.09 and 21, respectively (Table 4.3). Similarly for the sample B14VA-1, derived value of K and K_1 are 1275 MPa and 6.85 MPa (Figure 4.14a), respectively whereas for the sample B14VA-2 are 1750 MPa and 4.97 MPa, respectively (Figure 4.14b). The derived n and n_1 for sample B14VA-1 are 0.52 and 2.45, respectively, whereas for the sample B14VA-2 are 0.089 and 4.90, respectively (Table 4.3).

Table 4.3 Work hardening parameters derived from Ludwigson relationship

Alloys	K (MPa)	n	K_1 (MPa)	n_1	R^2	χ^2
B12VA-1	7397	0.75	6.68	-0.99	0.99	40
B12VA-2	2337	0.09	0.16	21	0.99	66
B14VA-1	1275	0.52	6.85	2.45	0.99	1
B14VA-2	1750	0.089	4.97	4.90	0.99	19

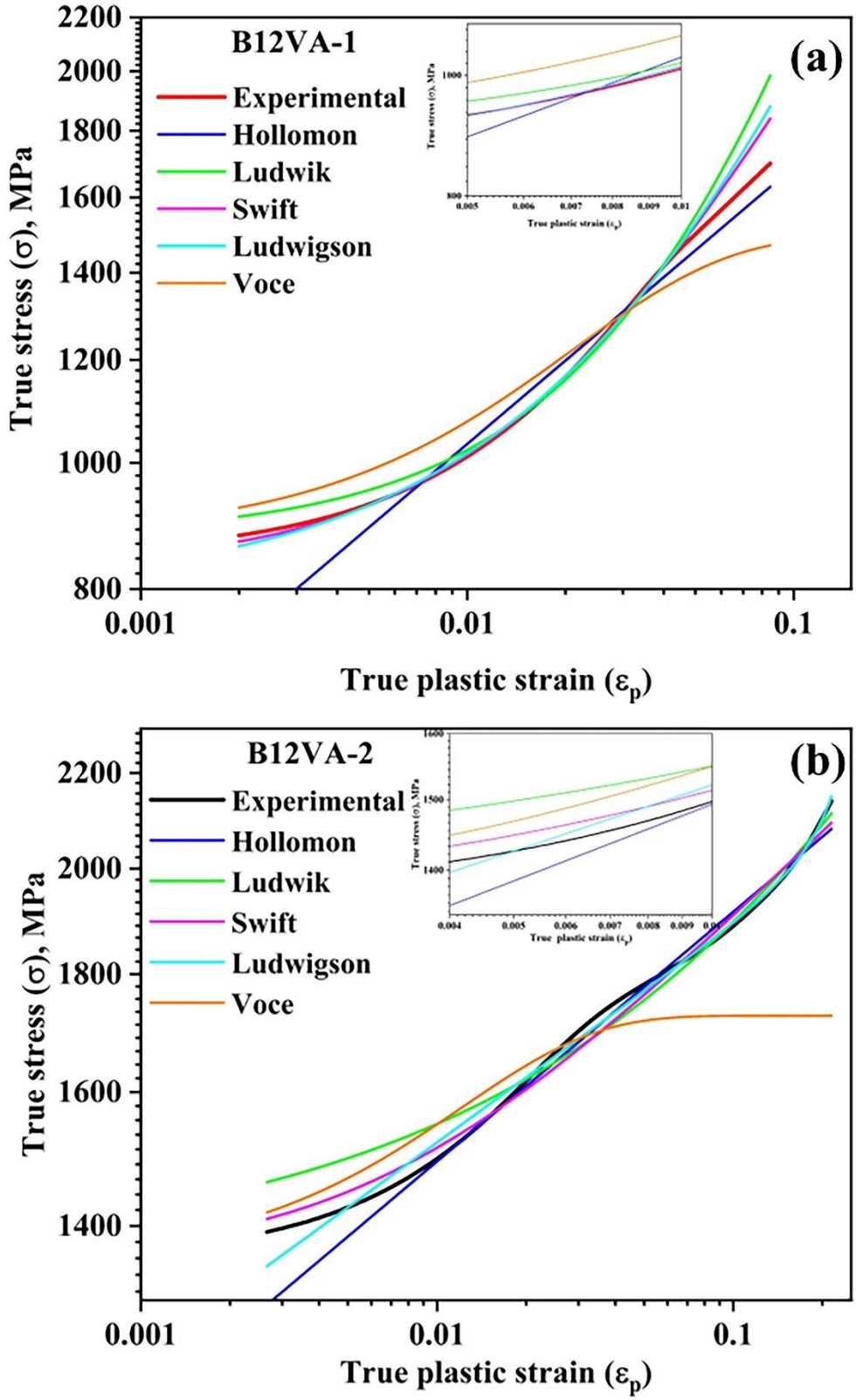

Figure 4.13 Logarithmic (base 10) true stress vs. logarithmic true plastic strain plots of (a) B12VA-1 and (b) B12VA-2 steels with respective fitting curves.

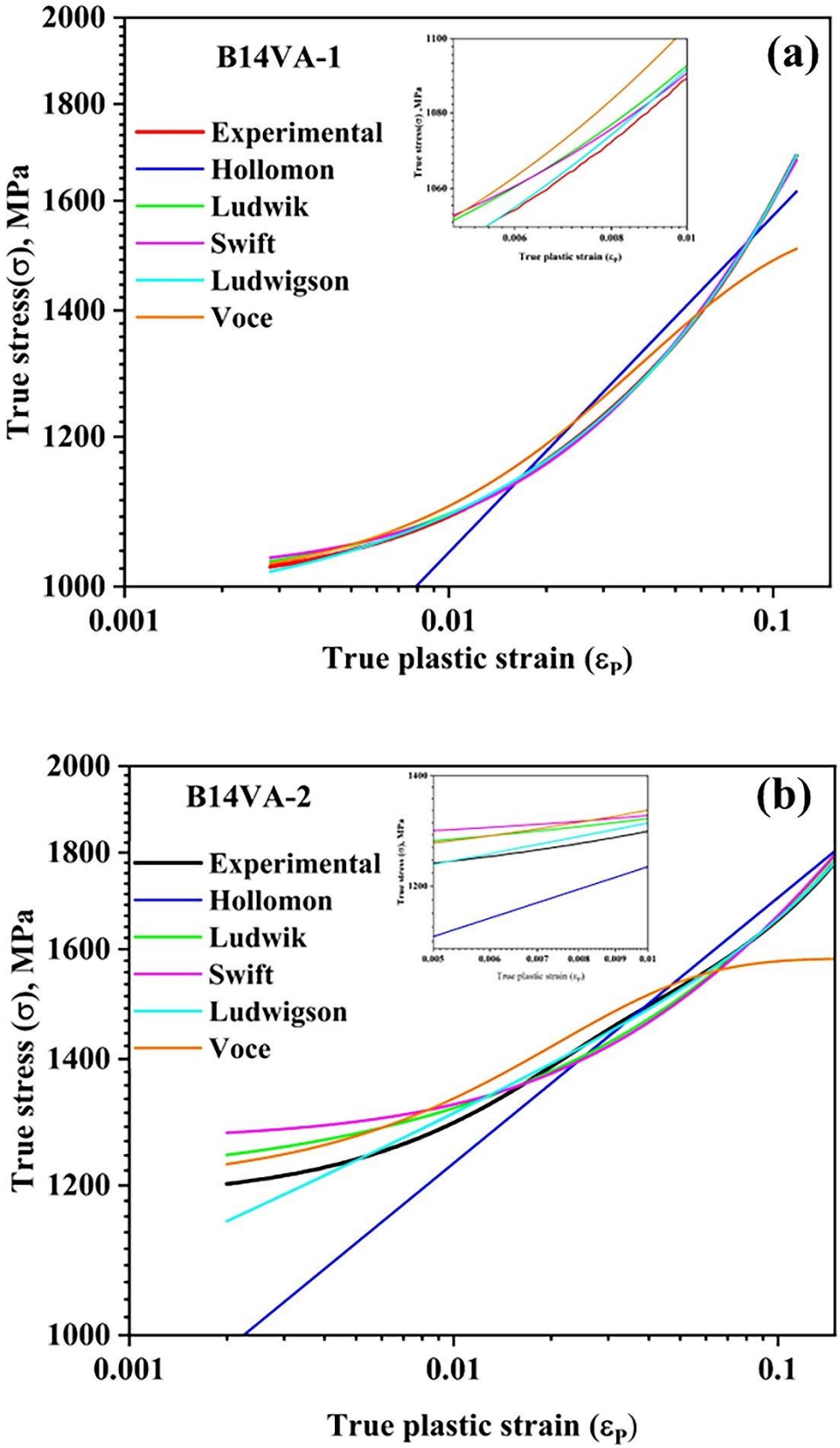

Figure 4.14 Logarithmic (base 10) true stress vs. logarithmic true plastic strain plots of (a) B14VA-1 and (b) B14VA-2 steels with respective fitting curves.

The double logarithmic plot of true stress- true plastic strain curve obtained from the Swift relationship provides the best fit with the experimental data, with the highest R-square values and lowest chi-square (χ^2) (Table 4.4) for both B15VA-1 & B15VA-2 steels (Figure 4.15a and Figure 4.15b) in comparison to respective values obtained from the Hollomon, Ludwik, Ludwigson and Voce equations. The derived strength coefficient and strain hardening exponent derived for B15VA-1 are 3560 MPa and 0.29, respectively. Also, the value of prior strain (ε_0) in the material is 0.029 (Table 4.4). The calculated flow stress ($K(\varepsilon_o)^n$) (when ε=0) from the derived work hardening parameters is 1275 MPa which is nearest to 0.2% YS (1281MPa). The strength coefficient and strain hardening exponent for B15VA-2 is 2496 MPa and 0.11, respectively. The amount of prior strain is 0.005. The estimated flow stress (when ε=0) using work hardening parameters is 1405 MPa which is nearest to 0.2% YS (1428 MPa). The sample B15VA-1 showed appreciable work hardening due to the TRIP effect, but sample B15VA-2 showed negligible work hardening due to the presence of strong retained filmy austenite enriched with carbon. The ductility is enhanced in B15VA-1 due to high work hardening and delayed necking to higher strain.

Table 4.4 Work hardening parameters derived from Swift relationship.

Materials	K MPa	ε_0	n	$K(\varepsilon_0)^n$ MPa	YS MPa	χ^2	R^2
B15VA-1	3560	0.029	0.29	1275	1281	12.9	0.99
B15VA-2	2496	0.005	0.11	1405	1428	147	0.99

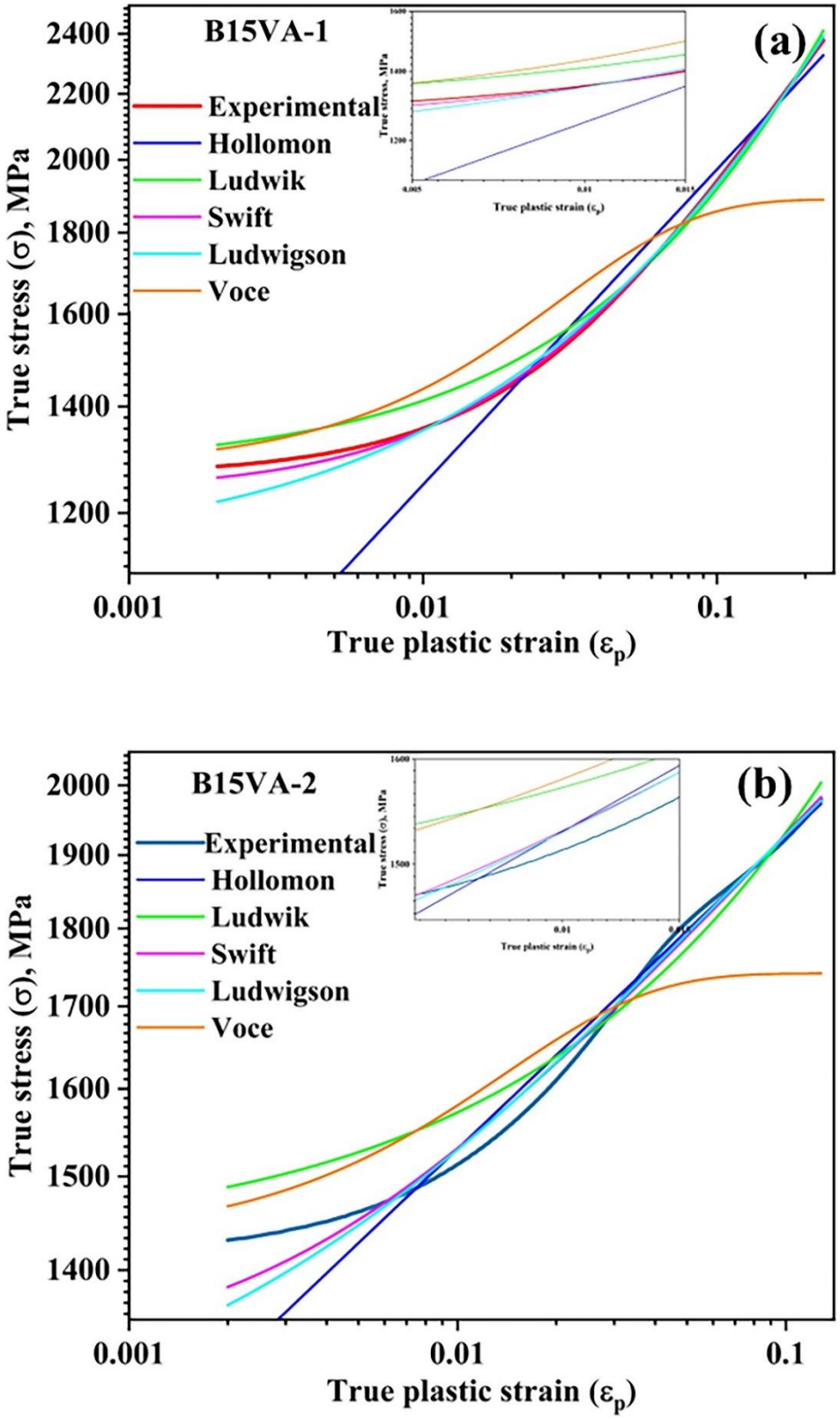

Figure 4.15 Logarithmic (base 10) true stress vs. logarithmic true plastic strain plots of (a) B15VA-1 and (b) B15VA-2 steels with respective fitting curves.

Work hardening behaviour of alloys B12VA-1, B12VA-2, B14VA-1 and B14VA-2 is also characterized by the rate of work hardening (θ) as a function of true stress (σ). Figure 4.16 shows the plot of instantaneous θ vs. σ for B12VA-1, B12VA-2, B14VA-1 and B14VA-2 samples, the values are obtained by numerical differentiation of the true stress corresponding to logarithmic strain, displaying three stages of θ variation for above mentioned samples. The value of θ decreased with increase in σ for all the samples. The work hardening behaviour of B12VA-1 can be categorized into three distinct stages. In Stage I, there is a gradual decline in the work hardening rate (θ). This is followed by a significant drop in the θ value during Stage II, as depicted in Figure 4.16a. At the end of Stage I, the true stress reaches 1319 MPa, indicating the stress level corresponding to a transition in the deformation behaviour (σ_1). Concurrently, the work hardening rate (θ_1) at this point measures 13573 MPa (Table 4.5). The conclusion of Stage II is marked by a true stress value (σ_2) of 1564 MPa, accompanied by a work hardening rate (θ_2) of 2802 MPa. Moving into Stage III, a softening stage, a steady-state variation of θ is observed. The true stress (σ_2) at the end of Stage III measures 1697 MPa, while the work hardening rate (θ_3) equals 1826 MPa (Table 4.5). These stages represent the distinct phases of work hardening in B12VA-1, each characterized by specific stress and work hardening rate values. Similar trend is followed for sample B12VA-2 but slightly higher slopes were observed. The true stress and work hardening rate corresponding to the end of stage I are 1597 MPa & 11666 MPa, stage II are 1796 MPa & 2438 MPa and stage III are 2139 MPa & 2484 MPa (Table 4.5).

Similarly, the work hardening behaviour of B14VA-1 is divided into three stages. Drastic fall in the θ in the Stage I is followed by gradual fall in the θ value in the stage II (Figure 4.16b). True stress value at the end of Stage I is 1073 MPa indicating the stress

corresponds to transition in the deformation behaviour (σ_1) whereas the value of work hardening rate (θ_1) at the end of stage I is 8863 MPa (Table 4.5). σ_2 indicates the end of the stage II and its value is 1394 MPa whereas the value of θ_2 is 5289 MPa. StageIII is softening stage in which steady state variation of θ is observed and the value of true stress(σ_2) at the end of stage III is 1687 MPa and θ_3 is 4632 MPa (Table 4.5). Similar trend is followed for sample B14VA-2 but slightly higher slopes were observed. The true stress and work hardening rate corresponding to the end of stage I are 1381 MPa & 8012 MPa, stage II are 1517 MPa & 3205 MPa and stage III are 2012 MPa & 2516 MPa (Table 4.5).

Table 4.5 Work hardening parameters of transition stress and work hardening rates.

Materials	Transition stress (σ_i)			Work hardening rate (θ_i)		
	σ_1	σ_2	σ_3	θ_1	θ_2	θ_3
B12VA-1	1319	1564	1697	13573	2802	1826
B12VA-2	1597	1796	2139	11666	2438	2484
B14VA-1	1073	1394	1687	8863	5289	4632
B14VA-2	1381	1517	2012	8012	3205	2516

Differentiation of Equation (4.3) with respect to ε and natural logarithmic of differential form gives

$$\ln\left(\frac{d\sigma}{d\varepsilon}\right) = \ln(kn) + (n-1)\ln(\varepsilon_o + \varepsilon) \qquad (4.6)$$

The work hardening behaviour of B15VA steel is evaluated by plotting the natural logarithm of work hardening rate ($\ln(\theta) = \ln(d\sigma/d\varepsilon)$) as a function of $\ln(\varepsilon_o+\varepsilon)$. The value of θ is calculated by numerical differentiation of true stress and corresponding true plastic strain. Figure 4.17 displays the plot of $\ln(\theta)$ vs $\ln(\varepsilon_o+\varepsilon)$ for samples B15VA-1 and

B15VA-2. The work hardening behaviour of sample B15VA-1 is divided into three stages. The strain-hardening is characterized by a gradual decrease in instantaneous work hardening rate with corrected true plastic strain ($\varepsilon_o+\varepsilon$) at an early stage of deformation (stage I) followed by a decrease in θ in stage II at a higher rate than that of stage I.

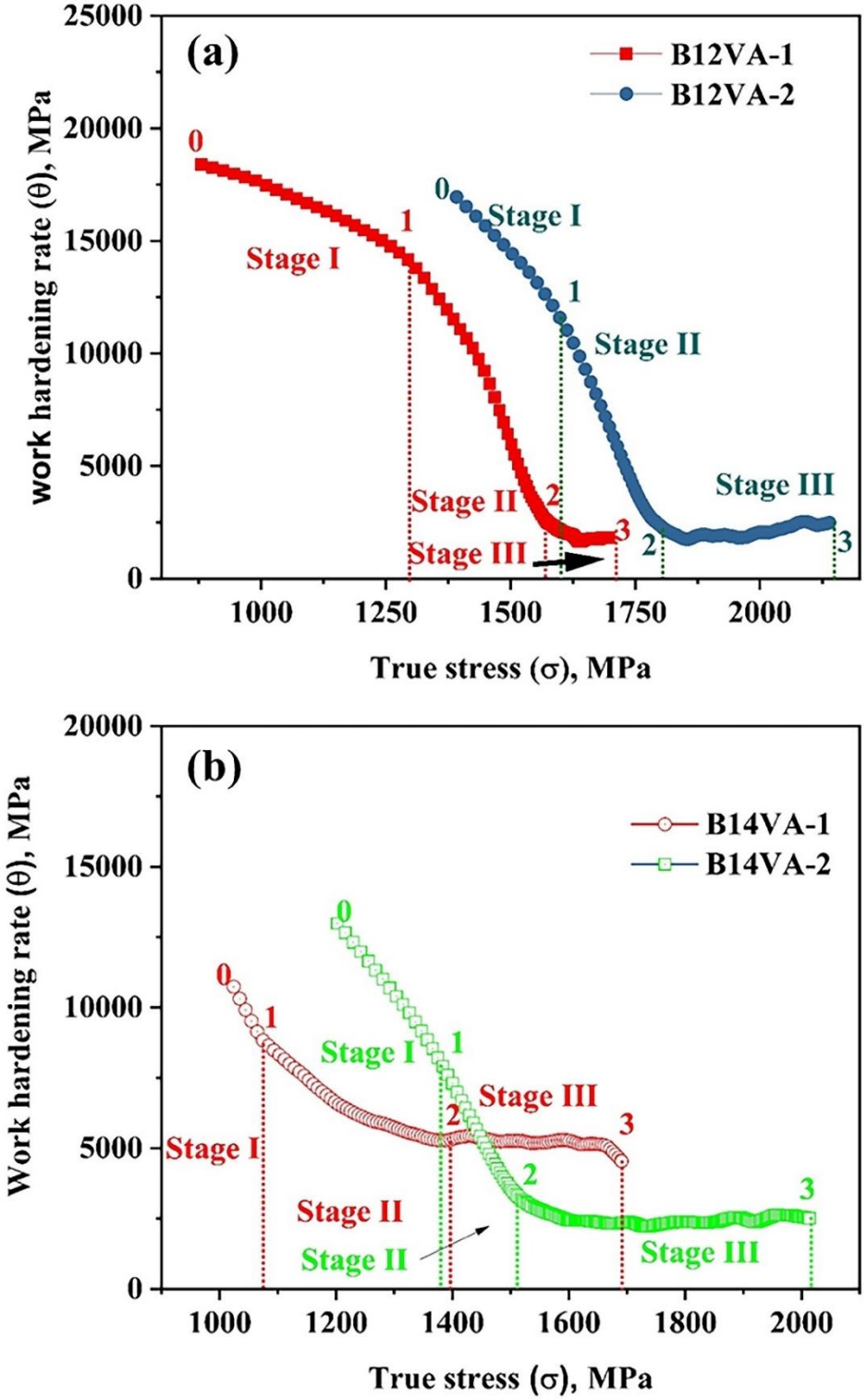

Figure 4.16 Variation of work hardening rate (θ) with the true stress: (a) B12VA-1 & B12VA-2, and (b) B14VA-1 & B14VA-2 samples.

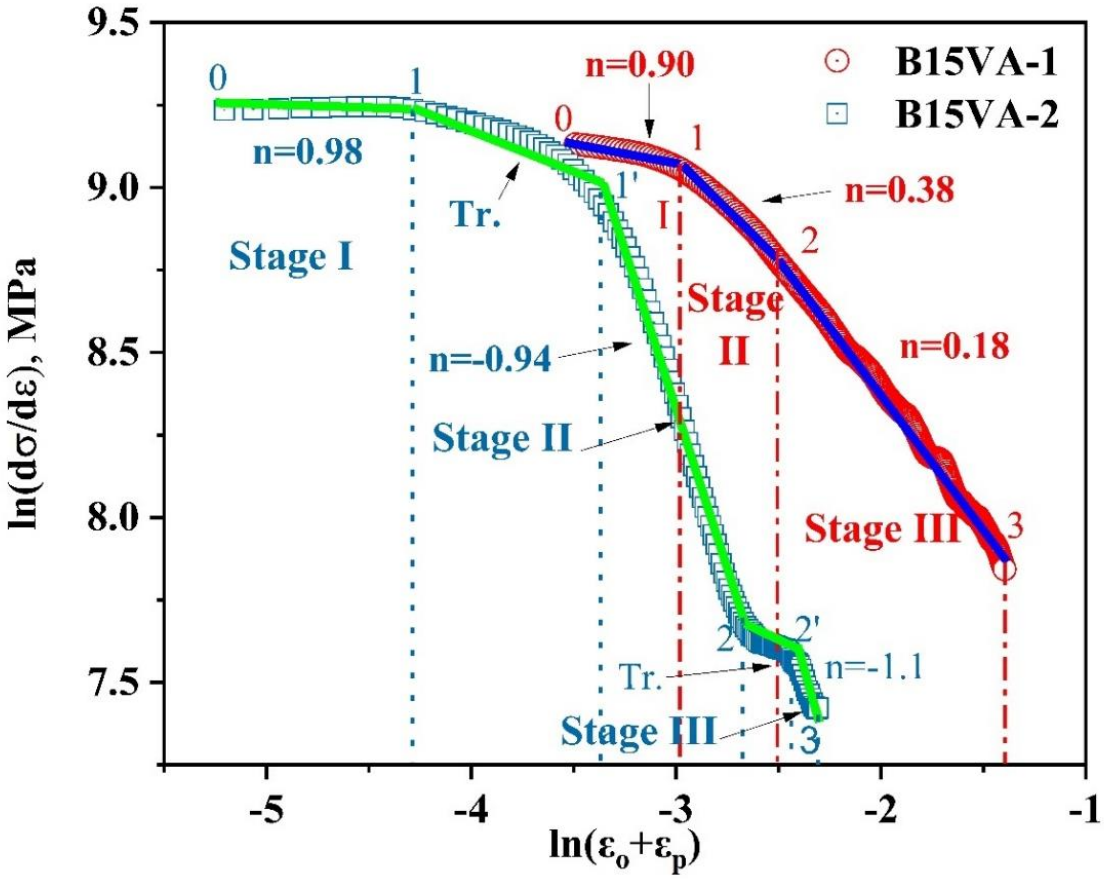

Figure 4.17 Variation of logarithmic work hardening rate (θ) with the logarithm of the sum of the true pre-strain and true strain for B15VA-1 and B15VA-2 samples

At the end of stage I(ε_1), the transition of the mechanism of strain hardening occurs at a true strain (ε_1) of 0.02. The slope of the transient stage (stage I) is -0.10 and the magnitude is less than the slope of stage II (-0.62). Also, the transition of the mechanism of strain hardening occurs at the end of stage II at ε_2 of 0.05. The slope of stage III is -0.82 and the magnitude of which is much higher than that of stages I & II (Table 4.6). Stage III is a softening stage in which θ decreases rapidly but at a much faster rate than stage II. Work hardening exponents in stages I, II and III are 0.90, 0.38 and 0.18, respectively. The work hardening rate (θ) at the initial stage of deformation of 9298 MPa is the highest. With increasing true strain, it decreases. At the end of stages I, II and III the strain hardening rate becomes 8702 MPa, 6555 MPa and 2623 MPa, respectively.

Table 4.6 Work hardening parameters of different slopes, transition strains and work hardening rates

Materials	Slope (n-1)			Transition strain (ε_i)			Work hardening rate(θ_i)		
	I	II	III	ε_1	ε_2	ε_3	θ_1	θ_2	θ_3
B15VA-1	-0.10	-0.62	-0.82	0.022	0.052	0.219	8702	6555	2623
B15VA-2	-0.02	-1.94	-2.1	0.009	0.065	0.094	10283	2161	1615

Sample B15VA-2 with a lesser amount of blocky austenite also displays three stages in ln (work hardening rate) vs ln (true (pre-strain+strain) or corrected true plastic strain) plot with transition zones of significantly wide true strain level. The nature of the plot of B15VA-2 is very similar to that of B15VA-1. The slope in stage I is very low but the slopes of stage II and stage III are much higher than that of B15VA-1(Figure 4.17 and Table 4.6). The numerical value range of stress corresponding to the transition in deformation (1-1') is 10283-8181 MPa and the stress corresponding to the end of stage II is 2161 MPa. Stage III is a softening stage in which θ decreases rapidly.

4.6 DISCUSSION

The B12VA and B14VA alloys have significant carbon content in the starting material. The carbon content of retained austenite of B12VA-1 and B14VA-1 are 1.49 and 1.28%, respectively which makes retained austenite chemically stable and suppress the Ms temperature to further lower temperature. In-spite of having chemical stability small amount of blocky retained austenite transformed to martensite during tensile straining. Increasing austempering time led to increase in the carbon supersaturation in the retained austenite even though significant amount of SIM formed during tensile straining of samples B12VA-2 and B14VA-2.

In B15VA-1 the increase in carbon content of retained austenite of 1.15 mass %, leads to an increase in chemical stability of austenite and lowering of Ms temperature. Therefore, cooling the austempered steel of low carbon in austenite to room temperature leaves chemically stable but mechanically unstable retained austenite; hence, during tensile straining significant part of retained austenite gets transformed to strain-induced martensite. Carbon content in filmy austenite is much higher than that of blocky austenite because of its mechanism of formation due to which the blocky austenite is more mechanically unstable [159]. A major part of blocky austenite in B15VA-1 gets converted to SIM by tensile deformation but filmy austenite is mechanically stable. A very little amount of filmy austenite transformed to SIM (Table 4.2). Higher austempering time (in case of B15VA-2) produces a higher amount of bainitic ferrite which increases the carbon content [53] in austenite to 1.73 mass%. The chemical stability as well as mechanical stability of retained austenite in B15VA-2 is higher but the majority of the blocky austenite transforms to SIM. The filmy austenite almost remains unchanged.

4.6.1 Hardness and Tensile Behaviour

The hardness of austempered B12VA, B14VA and B15VA steels increases with austempering time due to an increase in the vol% of bainite. The hardness of austempered steel increases after tensile testing due to the formation of hard SIM in B12VA-1′, B12VA-2′, B14VA-1′, B14VA-2′, B15VA-1′ and B15VA-2′.

The hardness, yield strength and ultimate tensile strength of the B12VA and B14VA alloys increases with increasing austempering time due to increase in the bainite content, which leads to increment in hardness and the strength of the steels. Also, the chemically stable and mechanically less unstable blocky austenite contributes to ductility. Yield strength of the B15VA-1 is lower than that of B15VA-2 because the former

contains a lesser amount of bainitic ferrite than the latter. The ultimate tensile strength of B15VA-1 is higher than that of B15VA-2. This is due to the higher amount of SIM in B15VA-1 than that of B15VA-2 and a higher amount of work hardening in the former. SIM improves strength and hardness significantly.

The engineering stress-engineering strain curve shows remarkable elongation (both uniform and total elongation) with excellent work hardening in the sample having a large amount of blocky austenite. The sample B15VA-1 undergoes SIM transformation during tensile straining and contributes to excellent elongation through the TRIP phenomenon but sample B15VA-2 having a lesser vol% of blocky austenite showed reduced work hardening behaviour due to the presence of strong retained austenite enriched with carbon [55]. Necking was delayed due to continuous work hardening and therefore, uniform elongation was increased. Nanostructured bainitic steel can be made ductile by a suitable amount of blocky austenite. The nano-scale thickness of plates in nano-grained structures has a higher resistance to necking and plastic instability [160]. High strength and high work hardening with excellent elongation ensure high tensile toughness of 492 MJ/m^3 in B15VA-1. Despite higher yield strength, limited work hardening and elongation resulted in lower tensile toughness of 299 MJ/m^3 in B15VA-2.

In most of the published literature (Table 1.1) high amounts of nanostructured bainitic steels are produced with maximum filmy austenite and a negligible amount of blocky one to get high strength and high hardness. Filmy austenite is preferred for its higher chemical as well as mechanical stability to avoid stress- or strain-induced martensite formation. Martensite with high carbon and high vol % of nanostructured bainitic ferrite makes a material very brittle. In the present investigation, the novel composition of high carbon bainitic steel with a higher amount of blocky austenite having

sufficient chemical stability but less mechanical stability is designed to exploit the benefit of SIM for strengthening, ductilization, improved formability and energy absorption. In addition, the novel composition of bainitic steel with 0.43 mass% Ni makes blocky austenite more stable which delays the plastic instability during the plastic deformation. During tensile deformation, the blocky austenite gradually transformed into strain-induced martensite and imparts ductility and strength through a TRIP mechanism. The bainitic steel with higher blocky austenite provides better strength and higher ductility than the steel having a higher bainite fraction. The currently designed alloy reports the highest PSE value of 55.16 GPa% along with high strength, hardness and ductility.

In the present study, the microstructural parameters and mechanical properties of the investigated novel high carbon nanostructured bainitic steel having a high content of retained austenite are compared with developed high carbon bainitic steels with a low fraction of retained austenite as well as newly developed bainitic steels/alloys (Table 1.1, Table 4.1, Table 4.2). At the low temperature of austempering (200-250) of steel containing ~0.8%C [54], strength and hardness are higher than that of B15VA-1 of the present study, but ductility and product of strength and elongation (PSE) are very poor and much lower. The comparable properties are achieved by Mateo and Caballero [43, 50, 54] at an austempering temperature of 300°C for steel containing 0.8 % carbon. The yield strength is ~30-40 MPa lower, UTS is ~120-170 MPa lower and hardness is ~100-112 HV lower than that of B15VA-1 steel in the present investigation.

Shorter austempering time limits carbon segregation and prevents carbide precipitation, which provides chemical stability to austenite but maintains its mechanical instability [36, 43, 49-52, 161]. On deformation, strength is achieved by contribution from the bainitic ferrite as well as strain-induced martensite. In addition, good ductility and energy

absorbing power are resulted from the transformation-induced plasticity. The percentage of the low angle grain boundary (LAGB) increased and the corresponding high angle grain boundary (HAGB) decreased in all the tensile fractured samples. These findings suggest that the tensile straining process impacts the microstructure, resulting in the formation of new grain boundaries due to the formation of strain-induced martensite from blocky retained austenite and the reorganization of existing ones.

4.6.2 Work Hardening Behaviour

The presence of a large number of mobile dislocations created during displacive development of bainite, as well as an alternate arrangement of thin bainite plates and films of retained austenite, caused the steel to display continuous yielding behaviour and substantial work hardening.

The variation of work hardening rate versus true stress curve of the samples B12VA-1, B12VA-2 and B14VA-2 shows similar trend and depicts three stages of work hardening. Material B14VA-1 having very high content of retained austenite (67%) with coarser size (~4 μm) of blocky austenite depicts lesser slope of stage I to that of stage II due to uniform deformation of softer retained austenite.

The variation of logarithm hardening rate (θ) vs ln(pre-strain+true strain) curve of the B15VA-1 sample shows three stages of work hardening with sharp changes in slope, which is consistent with previous findings for ferrite-martensite and ferrite-bainite dual phase steels [162-165]. Softer retained austenite absorbs the major part of the strain during the initial stages of plastic deformation, which has been demonstrated experimentally [166-168]. The deformation of relatively softer retained austenite is thus attributed to homogeneous deformation or easy glide in stage I, which then transforms into strain-induced martensite in stage II. The slope in stage II is significantly higher than

that in stage I due to SIM. The higher slope in stage II is due to SIM which is plastically restrained by surrounding bainitic ferrite as a result of the volume expansion caused by the transformation of austenite to martensite [169]. Deformation of harder constituents and the dynamic recovery in bainitic ferrite, aided by the cross slip of mobile screw dislocations, can be correlated to stage III [170, 171]. Stage III is attributed to multiphase straining of bainitic ferrite and continued deformation of favorably oriented austenite (blocky) to SIM, as well as deformation of hard austenite (filmy). Constrained deformation of multi phases, high dislocation pile-up and various dynamic recovery processes are responsible for further enhancement in the slope of stage III.

The plot ln(work hardening rate (θ) vs ln(pre-strain+true strain) for the B15VA-2 sample displays similarly three stages of work hardening but there is a gradual transition between stages. In the material B15VA-2, the slope of stage I is much lower than that for B15VA-1. The slope of stage II is significantly higher than that for B15VA-1 due to a reduction in strain hardening by reduced SIM. The slope of stage III is significantly higher due to a lack of work hardening by a reduction in SIM and enhanced recovery of dislocations.

4.6.3 Tensile Fracture Behaviour

The presence of higher carbon content in B12VA and B14VA alloys led to further increase in carbon content in the retained austenite during longer austempering time, makes the material chemically stable and mechanically less unstable. The material shows brittle fracture behaviour in-spite of having higher austenite content. Cleavage facets, surrounded with tearing ridge and little amount of micro dimples confirm the brittle fracture behaviour.

Due to the presence of a substantial quantity of retained austenite, ductile fracture with microvoid coalescence occurred at room temperature in the B15VA-1. Large size dimples along with micro dimples and tearing ridges are seen in the SEM fractographs of tensile fractured samples. In the case of ductile fracture mode, a large number of dimples along with little cleavage facets are present. The appearance of dimples, tear ridges and cleavage facets confirmed the mixed mode of fracture. Fractography of both samples B15VA-1 & B15VA-2 shows a mixed mode of fracture i.e. ductile and brittle fracture modes. Intense dislocation debris in fractured tensile samples is due to the combined effect of shape change leading to plastic deformation and tensile straining [172]. In tensile fractured samples, B15VA-1 and B15VA-2, strain-induced martensite of ε type were seen in the blocky austenite region. Similar features were observed in tensile strained samples by Brackley and Murr [173, 174].

The steel of the present investigation falls in the group 3 category in which significant strengthening comes from SIM in addition to nanostructured bainitic ferrite to achieve appreciably high strength and hardness. The microstructures of investigated steel depict bainitic ferrite plate thickness in the range of 24-25 nm. The microstructures show retained austenite in the range of 35 to 45% in which filmy austenite ranges 8.3-9.8 % but significant blocky austenite of 25.3-36.8% (Table 4.2). Higher elongation in these steels is exploited from the TRIP effect of less mechanically stable blocky austenite content. As a result, group 3 steel of nanostructured bainitic ferrite of 55%-65% produced at the austempering temperature of 250°C displays tensile strength in the range of 1742-1889 MPa (Table 4.1), total elongation in the range of 18.7-29.2%, PSE values in the range of 32.57-54.78 GPa%. Indeed, by reducing the time of isothermal treatments of metastable austenite, a lower amount of bainite or higher amount of retained austenite,

which is chemically stable but mechanically unstable, has resulted in better mechanical properties. The presence of a higher volume fraction of blocky austenite leads to the formation of strain-induced martensite during tensile deformation showing TRIP behaviour and benefits in both strength and ductility before reaching the percolation threshold.

Mateo et al. [50] have processed a steel composition containing 0.98wt %C. The steel was austempered at 250 °C for 600 h or 25 days and found nanostructured bainitic ferrite of 63 %. Present authors have modified this composition marginally keeping carbon percentage almost the same and adding 1.39 % Co and 1.13 % Al. The steel was austempered at 250 °C for just 18 h and found nanostructured bainitic ferrite of 55%. The results are very encouraging in terms of acceleration of transformation kinetics. Only high transformation kinetics is not sufficient for industrialization. In literature, for various bainitic steel compositions, very high strength with high hardness is reported but these materials have very low ductility and low toughness or low product of strength and elongation (PSE) (Table 1.1). While high elongation and high toughness are achieved in a few nanostructured bainitic steels, they have very poor strength and low hardness (Table 1.1). For an application like armours on the frontline battlefield, it is demanded that the materials should have high strength, high hardness, high elongation, high toughness, or high PSE values. B15VA-1 provides a tensile strength of 1889 MPa, hardness of 602 HV, elongation of 29.2% and a very high PSE value of 55.16 GPa% [Table 4.1]. The tensile properties are measured at strain rate of 3.3×10^{-4} s^{-1}. The transformation kinetics and properties of B15VA-1 are encouraging for the above requirements for industrial applications like armour. The application of a material for armour also requires excellent

performance against impact, i.e., mechanical performance at high strain rates which needs to be evaluated in future.

4.7 CONCLUSIONS

The main conclusions drawn from this chapter are given as follows:

1. Yield strength of nanostructured bainite increases with increasing bainite content but ultimate tensile strength is mainly controlled by strain-induced martensite (SIM).
2. Chemically stable but mechanically unstable retained austenite undergo strain-induced martensitic transformation that leads to high ductility because of high work hardening rate and delay in onset of necking.
3. In B15VA-1, majority of blocky austenite undergo strain-induced martensitic transformation under tensile loading due to lesser carbon in it. However, the filmy austenite is chemically and mechanically stable.
4. SIM adds to ductility by transformation-induced plasticity and increases work hardening rate. High work hardening rate at higher strain delays the onset of necking which results in higher uniform plastic elongation. Therefore, material B15VA-1 shows 12% higher uniform plastic elongation than B15VA-2 even though the former has a higher UTS of 1889 MPa.
5. High carbon percentage in retained austenite of B12VA-1 and B14VA-1 makes it both chemically stable and mechanically less unstable in comparison with B15VA-1.
6. Limited strain-induced martensitic transformation restricts ductility of B12VA-1 and B14VA-1. In spite of much higher percentage of retained austenite, these materials show lesser ductility.

7. Work hardening behaviour of the selected nanostructured bainitic steel matches with the Swift model of three stages of deformation mechanism with increasing strain.
8. Bainitic-austenitic steel of selected composition fails by mixed mode of fracture but the ductile fracture predominates.
9. Hardness, yield strength, ultimate tensile strength and total elongation of the patented steel samples are much lower than that of austempered steel.